P-1053
December 31, 2013

LAr1-ND: Testing Neutrino Anomalies with Multiple LAr TPC Detectors at Fermilab

C. Adams[1], C. Andreopoulos[2], J. Asaadi[3], B. Baller[4], M. Bishai[5], L. Bugel[6], L. Camilleri[7], F. Cavanna[1], H. Chen[5], E. Church[1], D. Cianci[8], G. Collin[6], J.M. Conrad[6], G. De Geronimo[5], A. Ereditato[9], J. Evans[10], B. Fleming*[1], W.M. Foreman[8], G. Garvey[11], R. Guenette[12], C.M. Ignarra[6], C. James[4], C.M. Jen[13], B.J.P. Jones[6], J. Ho[8], L.M. Kalousis[13], G. Karagiorgi[7], W. Ketchum[11], I. Kreslo[9], V.A. Kudryavtsev[14], D. Lissauer[5], W.C. Louis[11], C. Mariani[13], K. Mavrokoridis[2], N. McCauley[2], G.B. Mills[11], Z. Moss[6], S. Mufson[15], M. Nessi[16], O. Palamara*[1], Z. Pavlovic[11], X. Qian[5], L. Qiuguang[11], R. Rameika[4], D.W. Schmitz*[8], M. Shaevitz[7], M. Soderberg[3], S. Söldner-Rembold[10], J. Spitz[6], A.M. Szelc[1], C.E. Taylor[11], K. Terao[7], M. Thomson[17], C. Thorn[5], M. Toups[6], C. Touramanis[2], V. Radeka[5], C. Rudolf von Rohr[9], N. Spooner[14], T. Strauss[9], L. Thompson[14], R.G. Van De Water[11], M. Weber[9], D. Whittington[15], B. Yu[5], G. Zeller[4], and J. Zennamo[8]

[1] *Yale University, New Haven, CT*
[2] *University of Liverpool, Liverpool, UK*
[3] *Syracuse University, Syracuse, NY*
[4] *Fermi National Accelerator Laboratory, Batavia, IL*
[5] *Brookhaven National Laboratory, Upton, NY*
[6] *Massachusetts Institute of Technology, Boston, MA*
[7] *Columbia University, Nevis Labs, Irvington, NY*
[8] *University of Chicago, Enrico Fermi Institute, Chicago, IL*
[9] *University of Bern, Laboratory for High Energy Physics, Bern, Switzerland*
[10] *University of Manchester, Manchester, UK*
[11] *Los Alamos National Laboratory, Los Alamos, NM*
[12] *University of Oxford, Oxford, UK*
[13] *Center for Neutrino Physics, Virginia Tech, Blacksburg, VA*
[14] *University of Sheffield, Sheffield, UK*
[15] *Indiana University, Bloomington, IN*
[16] *CERN, Geneva, Switzerland*
[17] *University of Cambridge, Cambridge, UK*

December 31, 2013

*Contact person

ABSTRACT

This Proposal seeks to continue the development of the short-baseline neutrino oscillation program at Fermilab with the construction of the Liquid Argon Near Detector, or LAr1-ND, to be located in an existing experimental enclosure 100 m from the Booster Neutrino Beam target. The physics program will contribute, in conjunction with MicroBooNE, to the interpretation of the MiniBooNE neutrino-mode anomaly and will enable additional tests of high-Δm^2 neutrino oscillations through both disappearance and appearance searches.

Leveraging the advanced design work performed for LBNE and the very recent experience of the MicroBooNE detector construction, the LAr1-ND project has the potential to move forward quickly. Due to the high event rate at the near location, significant physics output can be achieved with a relatively short run. Beyond this near-term program, LAr1-ND could also serve as the near detector in a three LAr TPC experiment capable of definitively addressing the existing anomalies also in antineutrinos and making precision measurements of high-Δm^2 neutrino oscillations.

In addition to the physics program, LAr1-ND, following the MicroBooNE model, will have a development program serving as an engineering prototype for LAr TPCs for long baseline CP-violation searches in the future (e.g.: LBNE).

Contents

Chapter 1

Introduction and Overview

Neutrino oscillations, for which convincing evidence has emerged in the last two decades [1], stand as one of the most important discoveries in particle physics. Through the phenomenon of oscillations, we are now presented with exciting new opportunities for continued discovery. First, large mixing between the three active flavors is definitely confirmed [2]. This opens the door to a new era of discovery in neutrino physics, including the opportunity to test for CP-violation in the lepton sector [3]. Searching for CP-violation among neutrinos is an important step in determining if leptogenesis [4] is a viable theory to explain the matter–antimatter asymmetry in the universe today. Second, there are measurements from neutrino experiments that may be hinting at exciting new physics, including the possibility of additional low-mass sterile neutrino states. Such results include the so-called "anomalies" from LSND and MiniBooNE, a re-analysis of the predicted reactor anti-neutrino flux suggesting a deficit of reactor neutrinos, and the analysis of calibration data taken by GALLEX and SAGE. The recent puzzling results from these experiments, which together suggest the existence of physics beyond the Standard Model, have piqued interest in the community for projects that can provide new inputs to eventually solve this puzzle [5]. While each of these results taken by themselves have statistical significance ranging from 2 to 4 σ, taken together they provide significant indications for oscillations or other new phenomena. Definitive evidence for sterile neutrinos would be a revolutionary discovery, with implications for particle physics as well as cosmology. Proposals to address these signals by employing reactor, accelerator, and radioactive source experiments are in the planning stages or underway worldwide. With the MicroBooNE experiment [6], currently under construction on the Booster Neutrino Beam, Fermilab will be the first to explore such intriguing anomalies with accelerator neutrinos. The present proposal aims to build upon a solid and realistic program and significantly extend the physics reach of the Booster Neutrino Beam by adding a small-scale liquid argon time projection chamber (LAr TPC) near detector, LAr1-ND.

The physics potential of the LAr1-ND detector stands on its own and is the focus of the present proposal. The combination of LAr1-ND and MicroBooNE will effectively contribute to the interpretation of the appearance signal observed by MiniBooNE in neutrino-mode and enable important additional opportunities to search for the existence of new physics through neutrino disappearance. However, LAr1-ND can also serve as a next step in a phased program to build a world-class short-baseline neutrino program at Fermilab. The full LAr1 experiment, previously presented in an LOI [7] and a Snowmass Neutrino Group white paper [8], could then definitively address the question of neutrino oscillations in the $\Delta m^2 \approx 1\text{eV}^2$ region with both neutrino and anti-neutrino beams. Starting with the LAr1-ND detector, this program also represents a valuable development project for the LAr TPC technology toward the next generation of neutrino experiments. Short-baseline beam experiments provide an ideal opportunity to develop this technology at increasing scales while producing important physics results and addressing a key open question in the field today.

This proposal is organized as follows. A brief reminder of the main characteristics of the LAr TPC technology for use in neutrino physics and an overview of the proposed staged short-baseline multi-LAr TPC program at Fermilab are presented in the remainder of this Chapter. Chapter 2 reviews the various short-baseline experimental anomalies in neutrino physics that motivate this program. The Booster Neutrino Beam (NuMI beam) fluxes at the on-axis (off-axis) different detector locations are described in Chapter 3. Chapter 4 presents the LAr1-ND detector design and Chapter 5 discusses the physics program of the LAr1-ND experiment. Chapter 6 contains the cost estimate and the time scale for the LAr1-ND project and Chapter 7 the conclusions. Finally, in two appendices we present the potential of the LAr1-ND detector for physics beyond the first phase being proposed here. Appendix A discusses the possibility of a search for dark matter with a period of beam off-target running of the Booster Neutrino Beam. Appendix B describes the physics reach of a three LAr TPC detector configuration with the addition of a kiloton-scale LAr TPC at 700 m in the future.

1.1 Liquid Argon TPCs for Neutrino Physics

Liquid argon time project chamber detectors (LAr TPCs) are particularly attractive for use in neutrino physics because of their exceptional capabilities in tracking, particle identification and calorimetric energy reconstruction. The idea of using such a device for neutrino detection was first proposed over 35 years ago [9]. Charged particles propagating in liquid argon ionize nearby atoms and the freed electrons drift under the influence of an electric field (∼500 V/cm) applied across the detector volume. At the detector boundary, planes of closely spaced sense wires (wire pitch in the 3-5 mm range) are used to collect the free charge. Signals read out on the wires are proportional to the amount of energy deposited

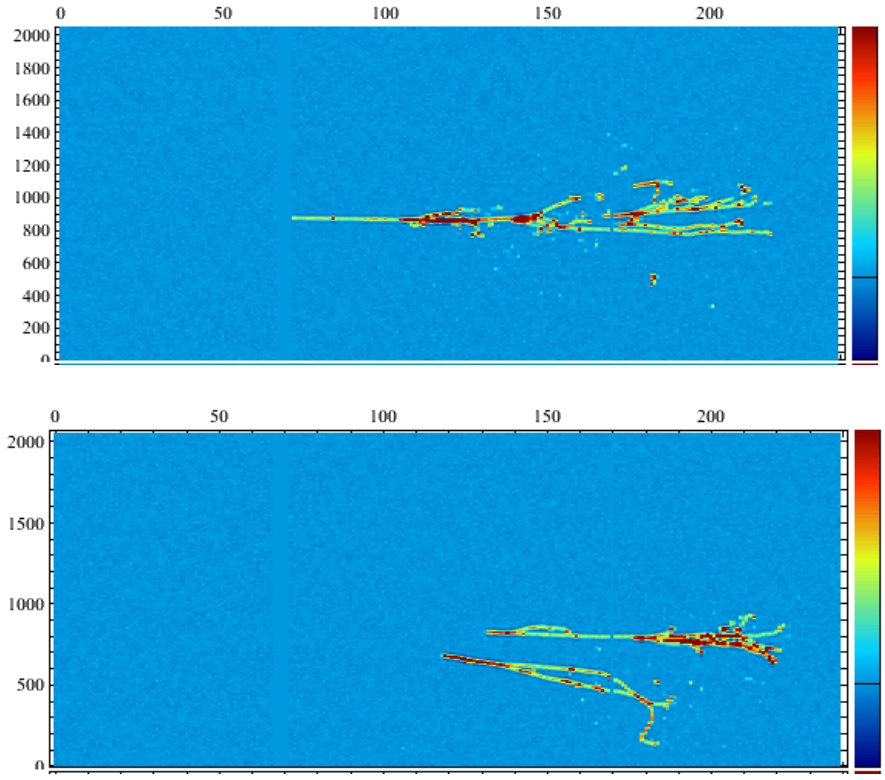

Figure 1.1: *Examples of simulated particle interactions in a LAr TPC detector illustrating the power to dustinguish electrons from photons. The top panel shows a single 1 GeV electron shower. The bottom panel shows the decay of a 1 GeV π^0 to two photons. The horizontal axis is the channel number on the collection wire plane. The vertical axis is the hit time and the color indicates the amplitude of the signal on the wires.*

in that spatial region.

The fine sampling and calorimetry enabled by this technology is key to its performance in neutrino physics. Cherenkov detectors, such as MiniBooNE and Super-K, are not able to distinguish electrons from single photons. An important advantage of the LAr TPC is the ability to separate electrons and photons by sampling the energy deposition before the buildup of an electromagnetic shower. When a photon converts to an e^+e^- pair, the resulting ionization in the first few centimeters is consistent with two minimum ionizing particles (mips), distinguishing it from the single mip deposit of an electron. Figure 1.1 compares a simulated single electron to a π^0 which has decayed to two photons. In the bottom figure, both photons from a π^0 decay are clearly visible in the event display, but, more importantly, the ionization strength near the beginning of each shower is approximately double that of the same portion of the electron shower in the top figure. π^0 decays are an important source

of background in searches for electron neutrinos, especially when one of the photons does not convert in the detector. The double mip deposition of converted photons allows even single photons to be identified, significantly reducing backgrounds in searches for ν_e appearance relative to other technologies.

1.2 A Staged Short-Baseline Multi-LAr TPC Program at Fermilab

The use of multiple detectors at different baselines presents a significant advantage for reducing systematic uncertainties in the measurement of neutrino oscillations; MINOS and Daya Bay are recent examples of the power of this approach [2]. The anomalous short-baseline results (discussed in Chapter 2) may be hinting at neutrinos oscillating with an amplitude 10 to 100 times smaller than those measured at Daya Bay and MINOS, thus emphasizing further the need for a multiple detector experiment in conducting a sensitive search for sterile neutrinos.

Fermilab has an opportunity to pursue such a multi-detector program using the superior event reconstruction capabilities of the LAr TPC technology through the construction of new detectors in the existing Booster Neutrino Beam. If the MiniBooNE neutrino mode excess [10, 11] is observed and its nature (electron or photon) established by MicroBooNE, then the immediate question becomes whether it is due to oscillations or produced in the proton target. This can be determined by a modest-scale LAr TPC detector at a nearer location, LAr1-ND. If an excess of electromagnetic events is *not* observed, this near detector can, in combination with MicroBooNE, rule out with better sensitivity the short-baseline oscillation explanation of the low energy excess at MiniBooNE and and fill in a crucial piece of the puzzle created by the existing anomalies. A near detector also extends the physics program in the Booster Beam by making possible a sensitive test of ν_μ disappearance through charged-current interactions, as well as a search for active flavor disappearance through neutral-current channels. These are critical aspects of a search for oscillations to sterile neutrinos and are only enabled with a near detector.

LAr1-ND is an 82 ton active volume LAr TPC to be located in the existing SciBooNE enclosure (at 100 m from the Booster Neutrino Beam target). The cryostat, cryogenics system, TPC and light collection systems, high voltage configuration and electronics readout will all serve as development steps toward LBNE. The membrane cryostat will house a CPA (Cathode Plane Assembly) and multiple APAs (Anode Plane Assemblies) to read out ionization electron signals. The front end electronics will build on the MicroBooNE and LBNE designs with cold pre-amplifiers multiplexed within LAr. The cryogenics system and

Figure 1.2: *Aerial view of the Fermilab Booster Neutrino Beam showing the locations of the MicroBooNE detector (currently under construction), the proposed LAr1-ND, and a possible future kiloton-scale LAr TPC detector, LAr1-FD.*

high voltage configuration will take advantage of that learned from LAPD (the Liquid Argon Purity Demonstrator), the 35 ton membrane cryostat prototype, and MicroBooNE. Overall, the design philosophy of the LAr1-ND detector is as a prototype for LBNE that functions as a physics experiment. While the present conceptual design described here is an excellent test of LBNE detector systems sited in a neutrino beam, the LAr1-ND collaboration is exploring innovations in this design and the opportunity to test them in a running experiment. LAr1-ND is an opportunity, therefore, to further the development of the LBNE detector design.

In summer 2012, the LAr1 collaboration submitted a Letter of Intent [7] to the Fermilab PAC describing the physics reach of a 1 kton LAr TPC detector located at 700 m along the Booster Neutrino Beam to serve as a far detector for the MicroBooNE experiment. Figure 1.2

shows the locations of the MicroBooNE detector, the LAr1-FD detector and the LAr1-ND detector described here. Since the LAr1 LOI, the advantages of starting with LAr1-ND as a first phase both for timeliness and efficiency have become clear. LAr1-ND, in combination with MicroBooNE, will bring a compelling early physics program, decisive determination of the nature of the MiniBooNE neutrino anomaly, and serve as a development step toward LBNE both for hardware and software. A new project at this scale also provides an avenue for expanding expertise with LAr TPC detectors within the neutrino physics community and an opportunity for building international collaboration in U.S. experimental neutrino physics.

With the existing SciBooNE enclosure at the appropriate near location for the LAr1-ND program, advanced design work from both MicroBooNE and LBNE, and relatively modest cost, the LAr1-ND can be built quickly and given the envisioned fiducial volume, have a definitive result within one year. With this schedule, the data run can be concurrent with the final year of MicroBooNE data taking, opportunistically taking advantage of the already approved MicroBooNE run. This timeliness puts Fermilab in an excellent position to not only confirm or rule out MiniBooNE's neutrino anomaly, but be able to interpret it as an oscillation signal.

Chapter 2

Motivation: Short-Baseline Anomalies in Neutrino Physics

In this chapter we very briefly review the various experimental anomalies that hint at the possibility of new physics occurring in the neutrino sector. We include this description for completeness, but refer the reader to more thorough descriptions of these results and their interpretation, including [5, 12] and the references therein.

In recent years, experimental anomalies ranging in significance (2.8–3.8σ) have been reported from a variety of experiments studying neutrinos over baselines less than 1 km. Results from the LSND and MiniBooNE short-baseline $\nu_e/\bar{\nu}_e$ appearance experiments show anomalies which cannot be described by oscillations between the three standard model neutrinos (the "LSND anomaly"). In addition, a re-analysis of the anti-neutrino flux produced by nuclear power reactors has led to an apparent deficit in $\bar{\nu}_e$ event rates in a number of reactor experiments (the"reactor anomaly"). Similarly, calibration runs using ^{51}Cr and ^{37}Ar radioactive sources in the Gallium solar neutrino experiments GALLEX and SAGE have shown an unexplained deficit in the electron neutrino event rate over very short distances (the "Gallium anomaly").

LSND $\bar{\nu}_\mu \to \bar{\nu}_e$

The Liquid Scintillator Neutrino Detector experiment (LSND) was conducted at Los Alamos National Laboratory from 1993 through 1998. LSND used a decay-at-rest (DAR) pion beam to produce a beam of $\bar{\nu}_\mu$ between 20-53 MeV about 30 m from a liquid scintillator-based detector. $\bar{\nu}_e$ were detected through inverse beta decay (IBD) on carbon, $\bar{\nu}_e p \to e^+ n$. The signature of IBD events is a prompt positron followed by a 2.2 MeV γ produced when

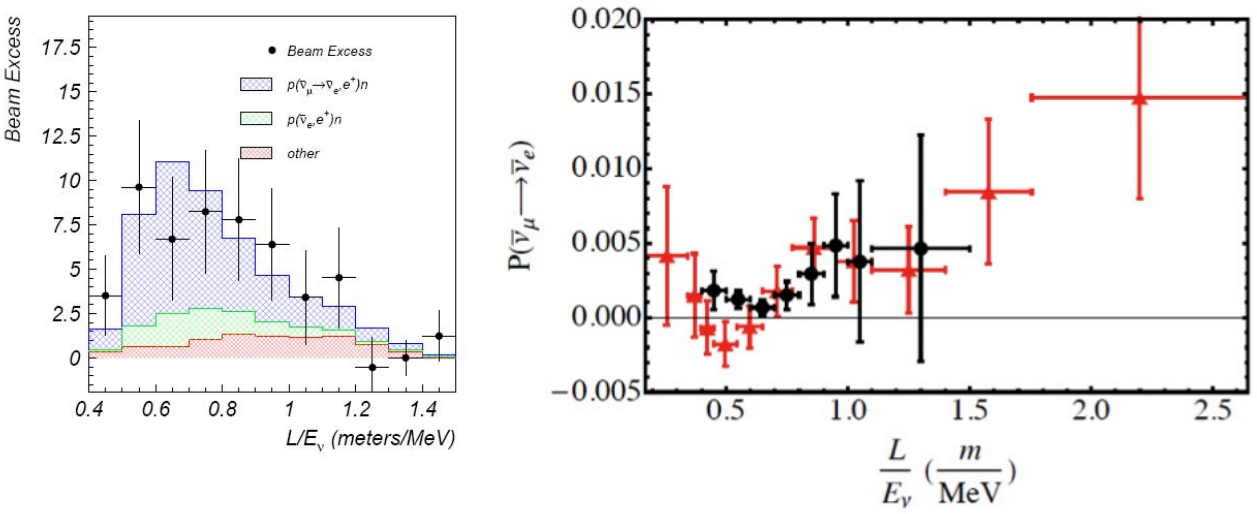

Figure 2.1: *Left: Excess of electron neutrino candidate events observed by the LSND experiment [13]. Right: Oscillation probability as a function of L/E_ν if the excess candidate events are assumed due to $\bar{\nu}_\mu \rightarrow \bar{\nu}_e$ transitions using MiniBooNE (red) and LSND (black) data.*

the neutron captures on free protons in the scintillator. After 5 years of data taking, $89.7 \pm 22.4 \pm 6.0$ $\bar{\nu}_e$ candidate events were observed above backgrounds, corresponding to 3.8σ evidence for $\overline{\nu}_\mu \rightarrow \overline{\nu}_e$ oscillations [13] occurring at a Δm^2 in the 1 eV^2 region. This signal, therefore, cannot be accommodated within the three Standard Model neutrinos, and like the other short baseline hints for oscillations at L/E_ν ~1 m/MeV, implies new physics.

MiniBooNE $\nu_\mu \rightarrow \nu_e$ and $\bar{\nu}_\mu \rightarrow \bar{\nu}_e$

The MiniBooNE collaboration has recently completed an analysis of their full ten year data set including both neutrino and anti-neutrino running [10, 11, 14, 15]. The MiniBooNE detector sits 540 m downstream of the Booster Neutrino Beam target at Fermilab. Predominately muon flavor neutrinos are produced in pion decay-in-flight, yielding a broad beam with peak energy around 700 MeV. Muon and electron neutrinos are identified in charged-current interactions by the characteristic signatures of Cherenkov rings for muons and electrons.

MiniBooNE observes a 3.4σ signal excess of ν_e candidates in neutrino mode (162.0 ± 47.8 electromagnetic events). These events, along with backgrounds, are shown in Fig. 2.2. The excess events can be electrons or single photons since these are indistinguishable in MiniBooNE's Cherenkov imaging detector. MicroBooNE will address this question at the same baseline as MiniBooNE by applying the LAr TPC technology to separate electrons and gammas.

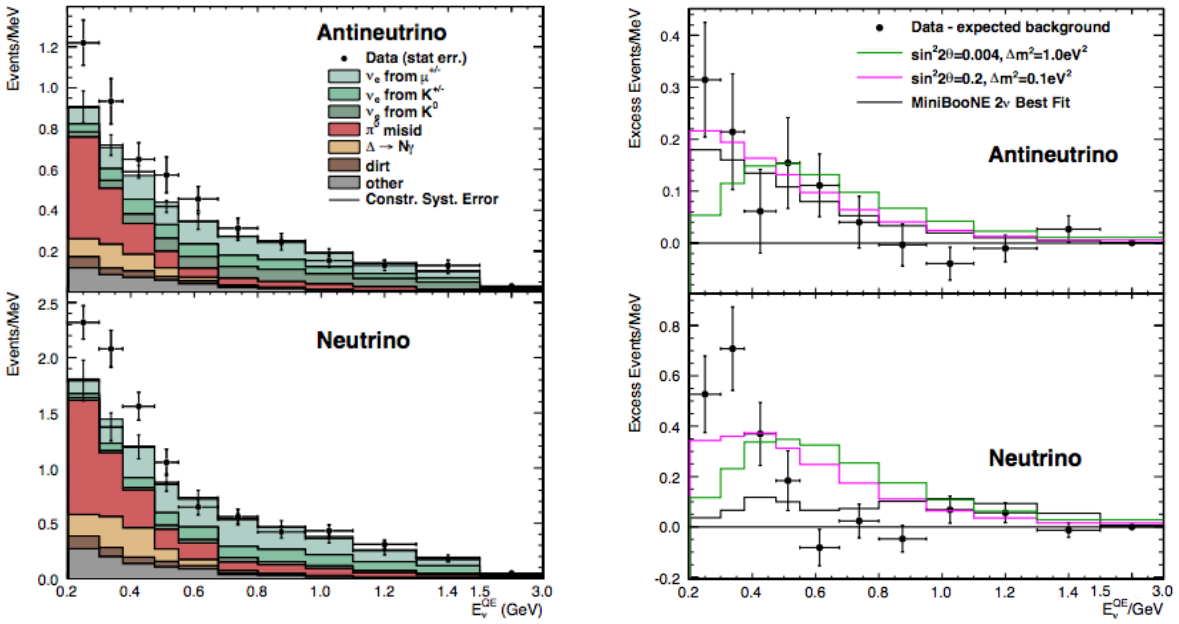

Figure 2.2: *Left: MiniBooNE $\bar{\nu}_e$ (top) and ν_e (bottom) candidate events and predicted backgrounds showing the observed excesses. Right: background subtracted event rates in anti-neutrinos (top) and neutrinos (bottom) [14].*

MiniBooNE also observes an excess of 78.4±28.5 electron anti-neutrino candidates (2.8σ) at both low and somewhat higher energies than in neutrinos as shown in Figure 2.2. Figure 2.1 compares the L/E_ν dependence of these events to the excess observed at LSND. It is this signal in anti-neutrino mode that the full multi-detector LAr1 experiment could address.

Reactor neutrino anomaly

A re-evaluation of the $\bar{\nu}_e$ flux produced by nuclear power reactors [16, 17] has prompted a re-analysis of short baseline reactor $\overline{\nu}_e$ disappearance measurements from the last several decades [18]. The new reference spectra takes advantage of a re-evaluation of inverse beta decay cross sections impacting the neutron lifetime, and accounts for long-lived radioisotopes accumulating in reactors. Figure 2.3 shows this predicted flux compared to reactor measurements as a function of the baseline of each experiment. With this new prediction, the observed rates of interactions in detectors between 10 and 100 meters from the reactors are, on average, 6-7% lower than that expected in the absence of oscillations. This result can be explained through $\bar{\nu}_e$ disappearance due to oscillations at $\Delta m^2 \sim 1$ eV^2, which could

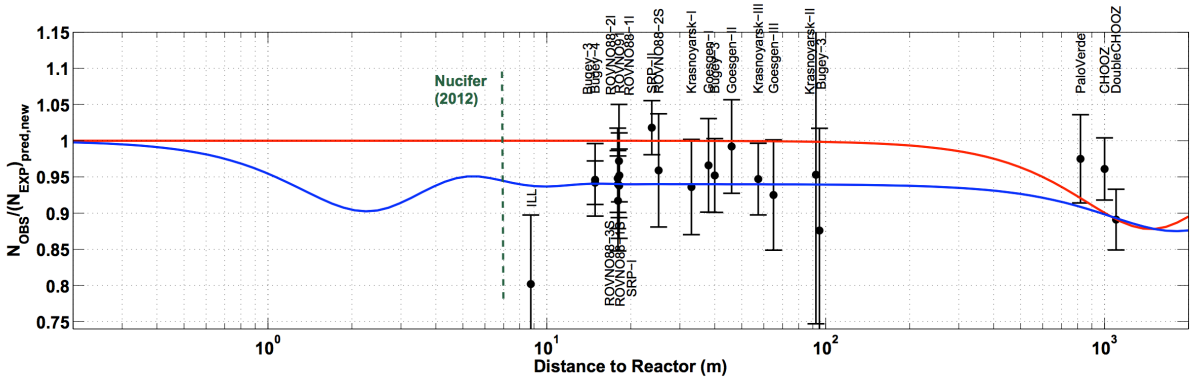

Figure 2.3: *Ratio of the observed to predicted reactor $\bar{\nu}_e$ rate for 19 different reactor neutrino experiments at baselines less that 100 m. The mean average ratio including correlations is* 0.927 ± 0.023*, indicating a 7.3% deficit at short baseline. The curves show fits to the data assuming standard three neutrino oscillations (red) and assuming 3+1 neutrino oscillations including one additional sterile neutrino (blue) [18].*

be consistent with the MiniBooNE and LSND appearance anomalies.

GALLEX and SAGE calibration data

Both the GALLEX and SAGE solar neutrino experiments used test sources to calibrate their detectors. In total they ran 4 test runs, 2 in GALLEX and 1 in SAGE with a ^{51}Cr source which emits a 750 keV ν_e, and 1 in SAGE with a ^{37}Ar source, an 810 keV ν_e emitter. The test data reveal a deficit of electron neutrinos relative to the predicted rate as shown in Figure 2.4. The best fit ratio of data to prediction is 0.86 ± 0.05 [19]. This deficit of very low energy electron neutrinos over very short baselines could also be explained through ν_e disappearance due to oscillations at $\Delta m^2 \geq 1$ eV^2.

Interpretation

Table 2.1 summarizes the results discussed above and lists their individual significance. While each of these measurements taken separately lack the significance to claim a discovery, together these signals could be hinting at important new physics. The most common interpretation is as evidence for the existence of one or more additional, mostly "sterile" neutrino states with masses at or below the few eV range. In these models, the mass states ν_1, ν_2 and ν_3 are those responsible for the well established oscillations observed at $\Delta m^2_{21} = 7.5 \times 10^{-5}$ eV^2

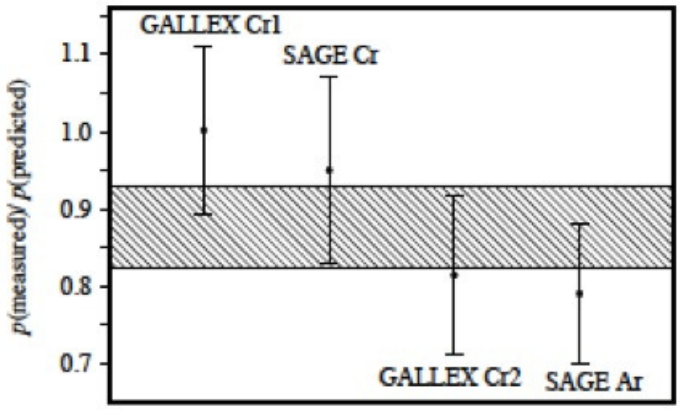

Figure 2.4: *The measured/predicted event ratio for GALLEX and SAGE source calibration data. The average, shown by the shaded band, is 0.86 ± 0.05 [19].*

Experiment	Type	Channel	Significance
LSND	DAR	$\bar{\nu}_\mu \to \bar{\nu}_e$ CC	3.8σ
MiniBooNE	SBL accelerator	$\nu_\mu \to \nu_e$ CC	3.4σ
MiniBooNE	SBL accelerator	$\bar{\nu}_\mu \to \bar{\nu}_e$ CC	2.8σ
GALLEX/SAGE	Source - e capture	ν_e disappearance	2.8σ
Reactors	Beta-decay	$\bar{\nu}_e$ disappearance	3.0σ

Table 2.1: *Summary of the experimental hints suggesting the possibility of high-Δm^2 neutrino oscillations.*

and $\Delta m^2_{31} = 2.4 \times 10^{-3}$ eV^2 and are taken to be dominated by active flavors (ν_e, ν_μ, ν_τ) with only small contributions from sterile flavors. Additional higher mass neutrino states, ν_4, ν_5, ... are taken as mostly sterile with small active flavor content (Fig. 2.5). The experimental results described above can be interpreted as indications of oscillations due to mass-squared splitting in the $\Delta m^2_{41} \approx [0.1 - 10]$ eV^2 range.

Given the importance of such a discovery, it is clear that the existing anomalies must be explored further by repeating the existing measurements in an effective way capable of addressing the oscillation hypothesis.

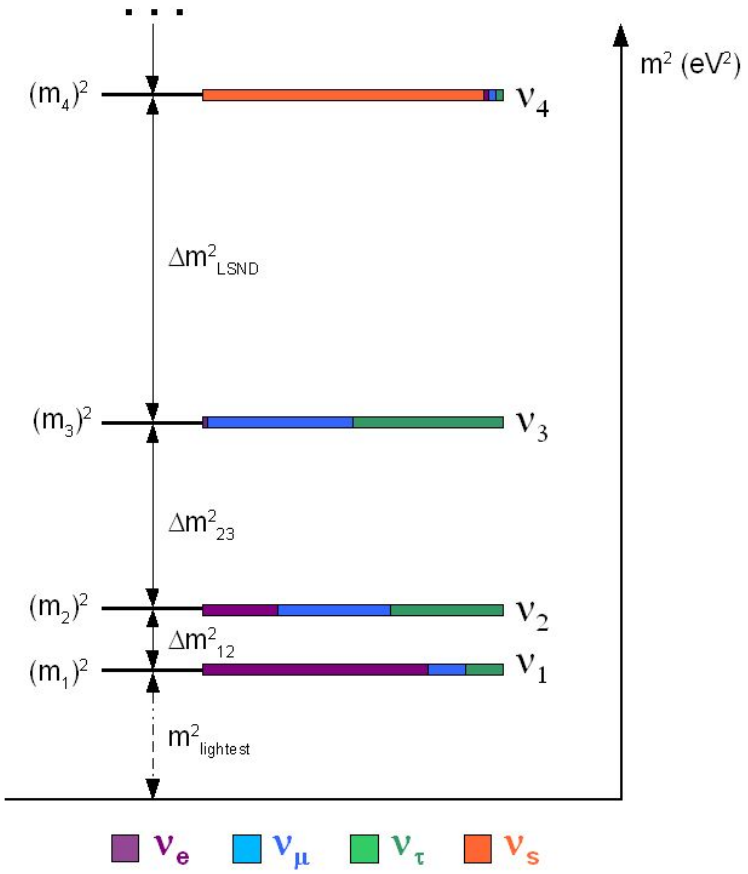

Figure 2.5: *Possible hierarchy of neutrino masses with 3 active and 1 (or more) sterile neutrinos. The LSND and other anomalous results are often interpreted as evidence for an order 1 eV^2 neutrino state that is mostly sterile.*

Chapter 3

Neutrino Beams

The primary source of neutrinos for LAr1-ND is the Booster Neutrino Beam (BNB). This same beamline has been used with the MiniBooNE experiment and will be used with the MicroBooNE experiment. This proposal assumes no changes to the BNB beamline design. In addition to the on-axis BNB flux, the detectors would be exposed to an off-axis component of the Neutrinos at the Main Injector (NuMI) beamline. Figure 3.1 shows the locations of the different detectors and the two FNAL neutrino beamlines. The NuMI event samples will provide an opportunity to study neutrino interactions in liquid argon over a broader energy range than that provided by the Booster Beam alone.

3.1 The Booster Neutrino Beam

Neutrinos in the BNB are produced by impinging 8 GeV protons on a beryllium target. A magnetic focusing horn is used to steer charged pions and kaons down a 50 m long open decay tunnel. The decay tunnel length can be shortened to 25 m by lowering a set of steel absorber plates suspended over the decay region at that location. The horn polarity can be set to focus either positive or negative mesons giving rise to either a predominantly muon neutrino or muon anti-neutrino beam. The $\nu_e/\bar{\nu}_e$ content of the beam is about 0.6% of the total flux integrated over all energies.

On-axis neutrino fluxes at the BNB are well known. Calculations are made with a Geant4-based Monte Carlo simulation provided by the MiniBooNE collaboration [20] that has been tuned using dedicated hadron production data from the HARP experiment [21] as well as the world's data on kaon production. Figure 3.2 shows the neutrino fluxes at the 100 m, 470 m and 700 m on-axis locations in the neutrino and anti-neutrino beam configurations of the BNB.

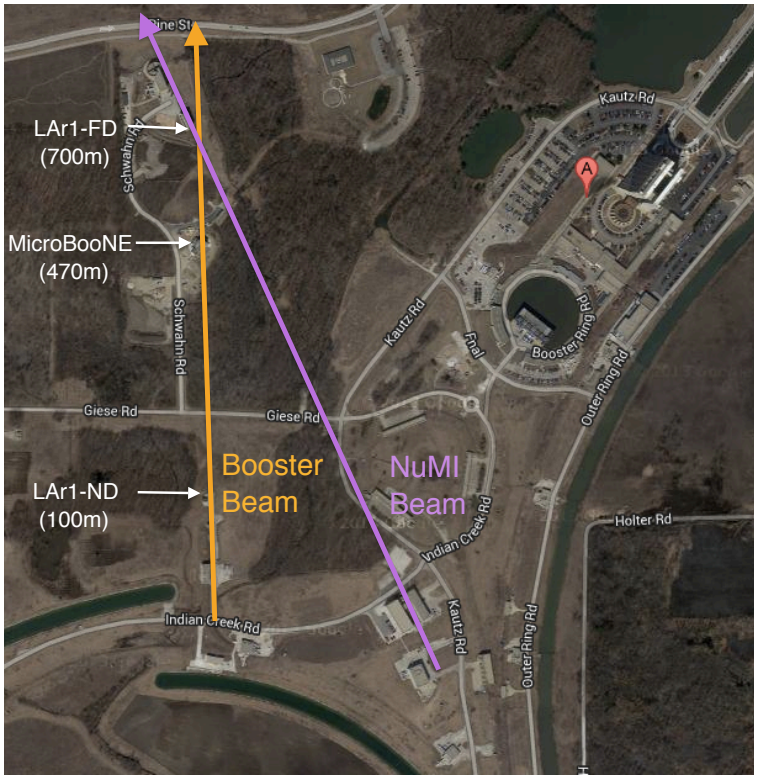

Figure 3.1: *Aerial view of the NuMI and Booster beams and the different detector locations.*

The predicted fluxes at locations beyond MicroBooNE have almost identical shapes, however some difference is expected when compared to the 100 m location due to its proximity to the neutrino source. Fig. 3.3 provides the ratios of the absolute fluxes as a function of neutrino energy in order to highlight differences in the shapes of the neutrino spectra. The ratio Φ(MicroBooNE)/Φ(LAr1-ND) is on the left and shows clearly the effect of LAr1-ND being only 50 m from the end of the decay region. The effect is more pronounced in the ν_μ spectrum, but note that the ν_e flux does fall off slightly faster than $1/r^2$ between these two locations ($100^2/470^2 = 0.045$). In contrast, the ratio Φ(LAr1-FD)/Φ(MicroBooNE) on the right indicates that the neutrino flux past MicroBooNE falls off almost exactly as $1/r^2$ at all neutrino energies ($470^2/700^2 = 0.45$).

3.2 The NuMI Neutrino Beam

Neutrinos in the NuMI beam are produced by impinging 120 GeV protons on a graphite target. Two magnetic focusing horns are used to steer charged pions and kaons down a 675

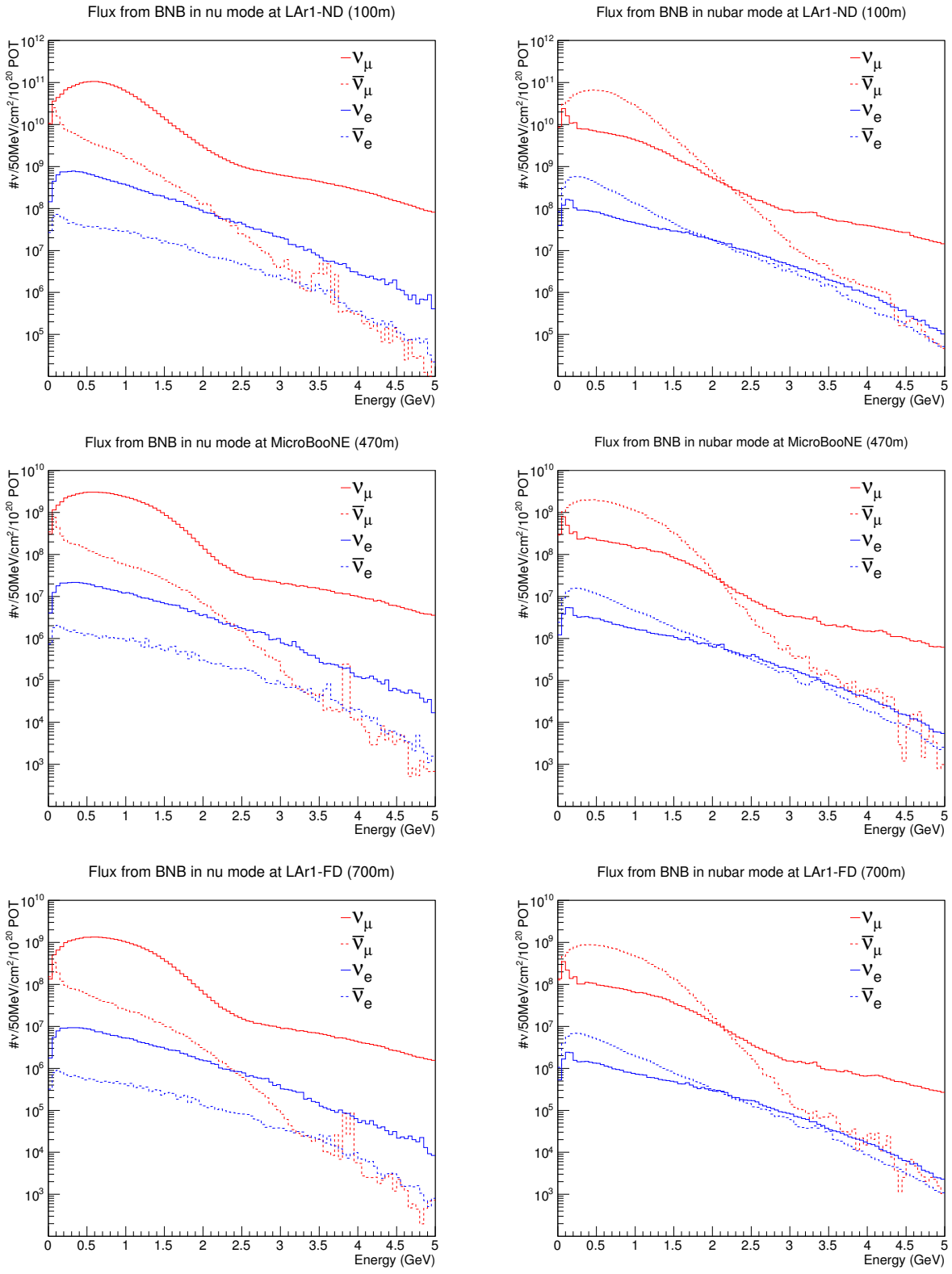

Figure 3.2: *Predicted fluxes from the on-axis BNB beam at the different detector locations: Top: LAr1-ND, Middle: MicroBooNE, Bottom: LAr1-FD. The left plots are for neutrino mode running and the right plots are for anti-neutrino mode running.*

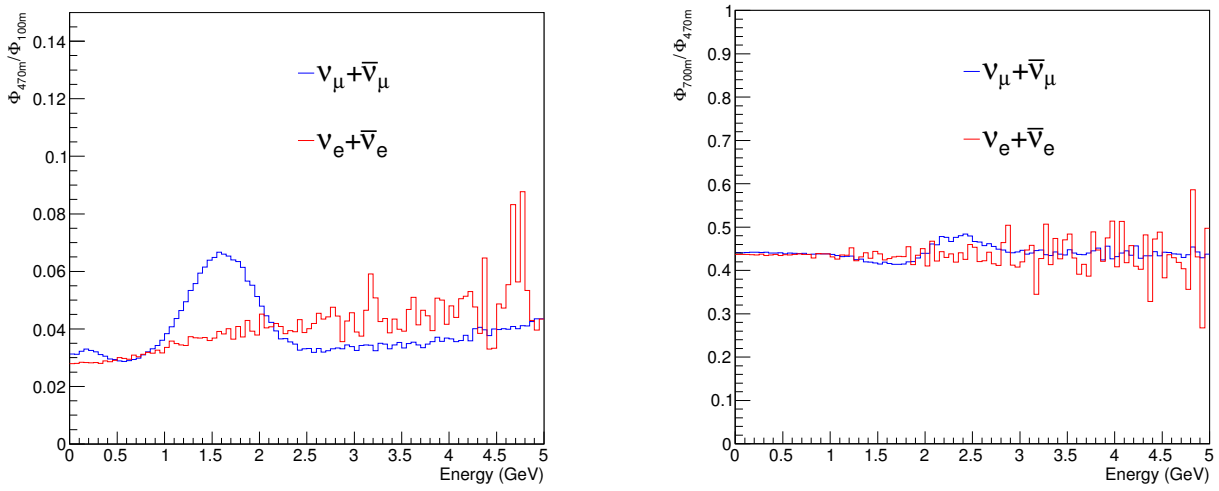

Figure 3.3: *Ratios of the muon type and electron type neutrino fluxes at different detector locations. The left panel compares the flux at MicroBooNE to the ones at LAr1-ND at 100 m. The right panel compares the flux at MicroBooNE to the ones at LAr1-FD at 700 m.*

m long open decay tunnel. The horn polarities can be set to focus either positive or negative mesons giving rise to either a predominantly muon neutrino or muon anti-neutrino beam. The NuMI beam will provide a large flux of off-axis neutrinos to the different detectors sitting on the BNB at the surface. The LAr1-ND detector is very off-axis at an angle of $\sim$30°, the MicroBooNE detector is $\sim$8° off-axis and the LAr1-FD is only $\sim$6° off-axis from the NuMI beamline (see Figure 3.1).

The predicted fluxes at the different detector locations are shown in Figure 3.4. The predicted event rates in each detector from the NuMI neutrino fluxes are presented in Section 5.3 and Appendix B.

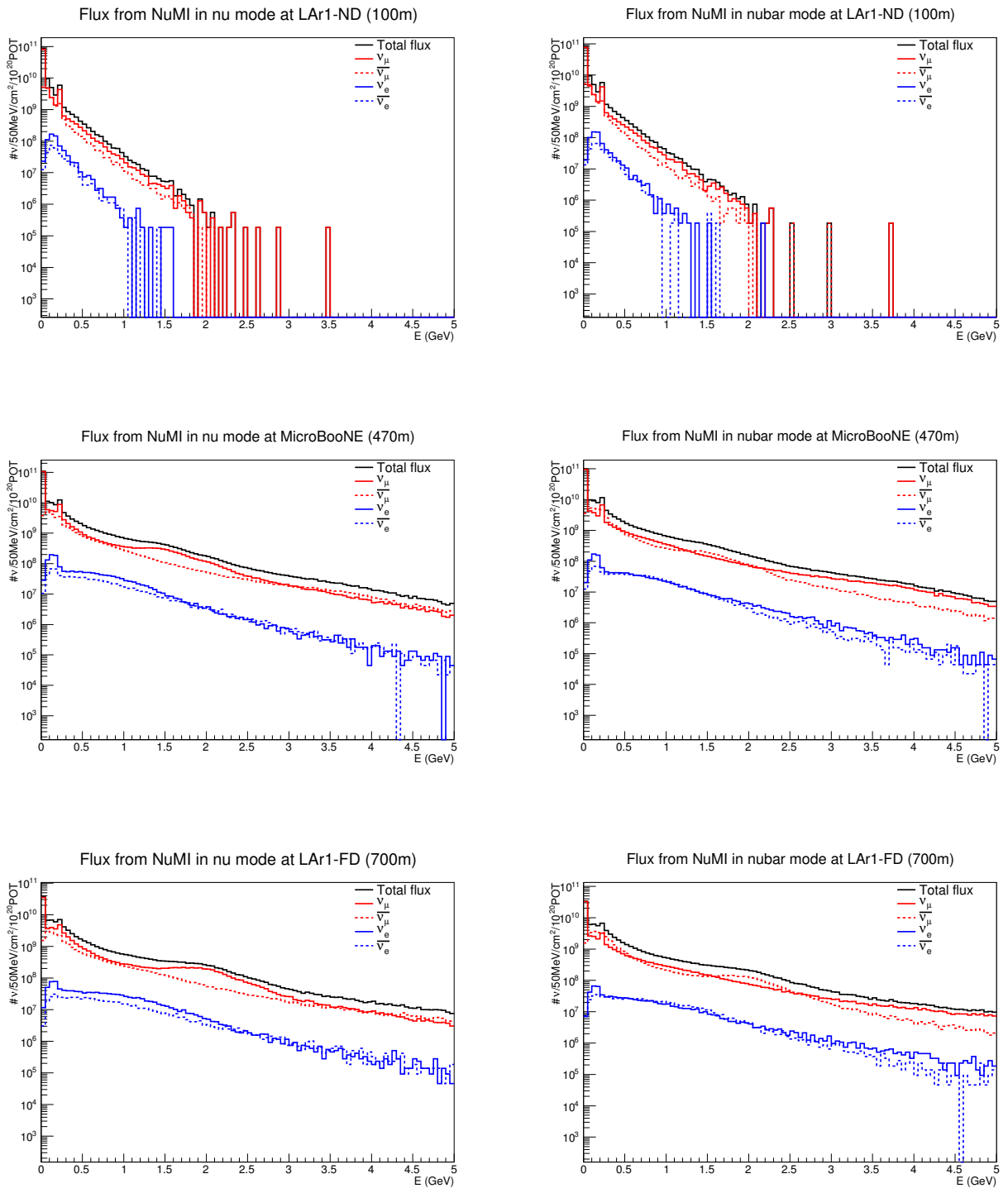

Figure 3.4: *Predicted fluxes from the off-axis NuMI beam at the different detector locations: Top: LAr1-ND, Middle: MicroBooNE, Bottom: LAr1-FD. The left plots are for neutrino mode running and the right plots are for anti-neutrino mode running.*

Chapter 4

LAr1-ND Detector

The design of the LAr1-ND detector builds on many years of LAr TPC detector R&D and experience from design and construction of ICARUS T600 [22], ArgoNeut [23], MicroBooNE and LBNE [24].

The basic concept for LAr1-ND is a membrane-style cryostat to be constructed in the experimental enclosure that previously housed the SciBooNE experiment. This design provides a safe and cost effective way to build large cryostats and cryogenics systems. LAr1-ND could also serve as a test bed to evaluate new concepts for the yet larger LAr TPCs that will enable future experiments. The major systems of the detector will provide opportunities to implement new designs, construction techniques, and, importantly, evaluate the physics performance of the design in a running experiment with large neutrino event samples. Located on-axis at 100 m from the Booster Neutrino Beam target, the existing enclosure provides an ideal location for a BNB near detector.

4.1 The SciBooNE Enclosure

The SciBooNE enclosure, shown in Fig. 4.1, is a below grade rectangular concrete structure with the following interior dimensions:

- Length (beam direction) = 4.9 m
- Width = 7.0 m
- Depth: floor-grade = 8.5 m, floor-ceiling = 11.6 m.

From the information provided by the Fermilab Facilities Engineering Services Section, the walls and floor of the SciBooNE enclosure are capable of withstanding the hydrostatic

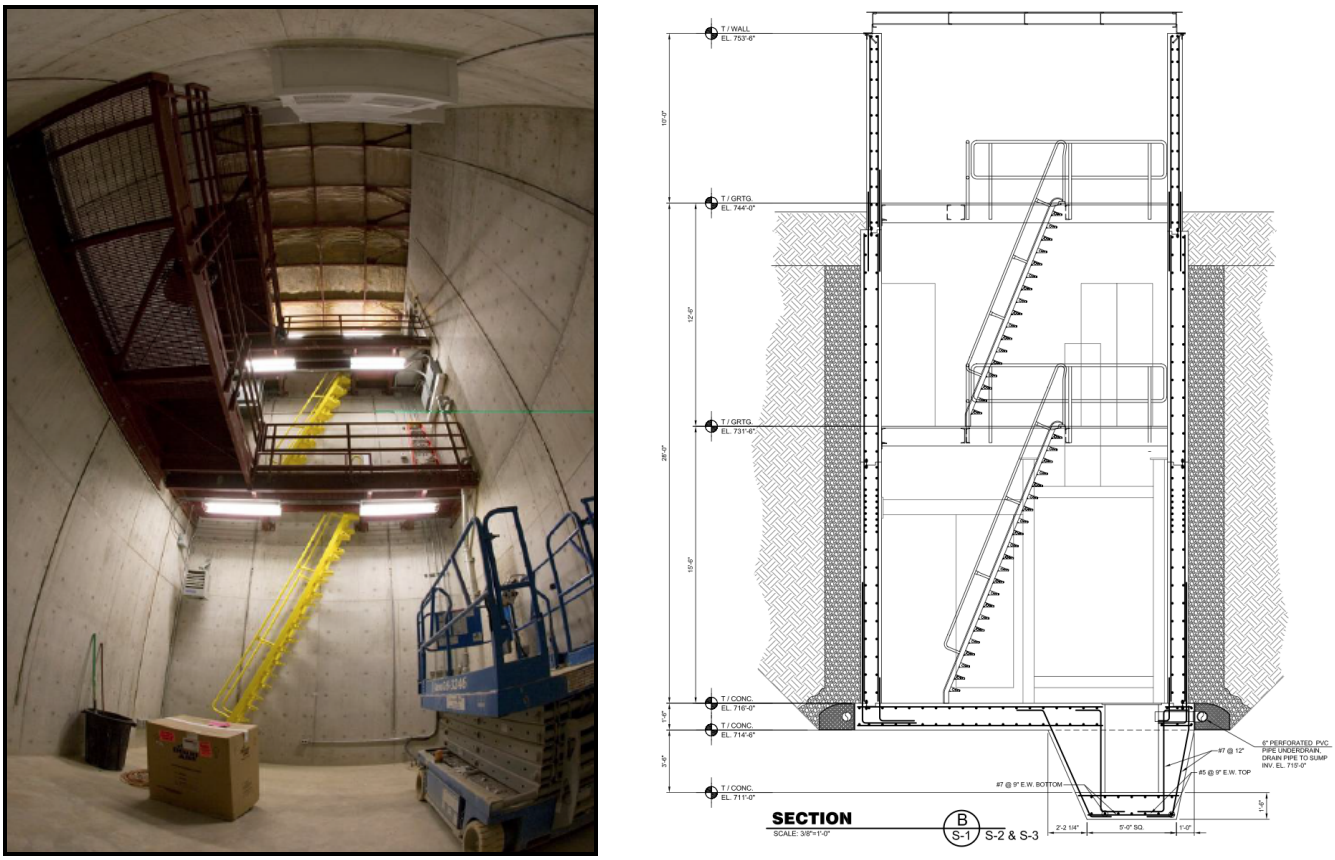

Figure 4.1: *(Left) The empty SciBooNE detector hall located at 100 m along the Booster Neutrino Beam. (Right) Side view of the SciBooNE enclosure. The neutrino beam enters from the right.*

pressures that would be generated by the LAr1-ND cryostat.

4.2 LAr1-ND Detector Design

Figures 4.2 and 4.3 present the basic schematic design for the LAr1-ND detector. A foam insulated, corrugated stainless steel membrane cryostat is constructed in the below-grade pit of the SciBooNE hall, supported by the outer concrete walls of the enclosure, and filling the entire length in the beam direction. On beam right shielding blocks are used to narrow the hall by 1 m. The blocks transfer the hydrostatic load of the cryostat to the outer walls. This configuration approximately centers the detector on the beam axis as seen in Fig. 4.3. The interior dimensions of the rectangular cryostat are 4.4 m long in the neutrino beam direction, 5.1 m wide and 4.8 m tall, amounting to 150 tons total of liquid argon. The active volume boundary, determined by the size of the anode (wire plane) and cathode assemblies,

is 3.65 m (beam direction) x 4.0 m (wide) x 4.0 m (tall) = 58.4 m^3 or 82 tons of argon. Fiducial volume selections will depend on the analysis, but for the ν_e analysis, for example, the fiducial mass is 49 tons.

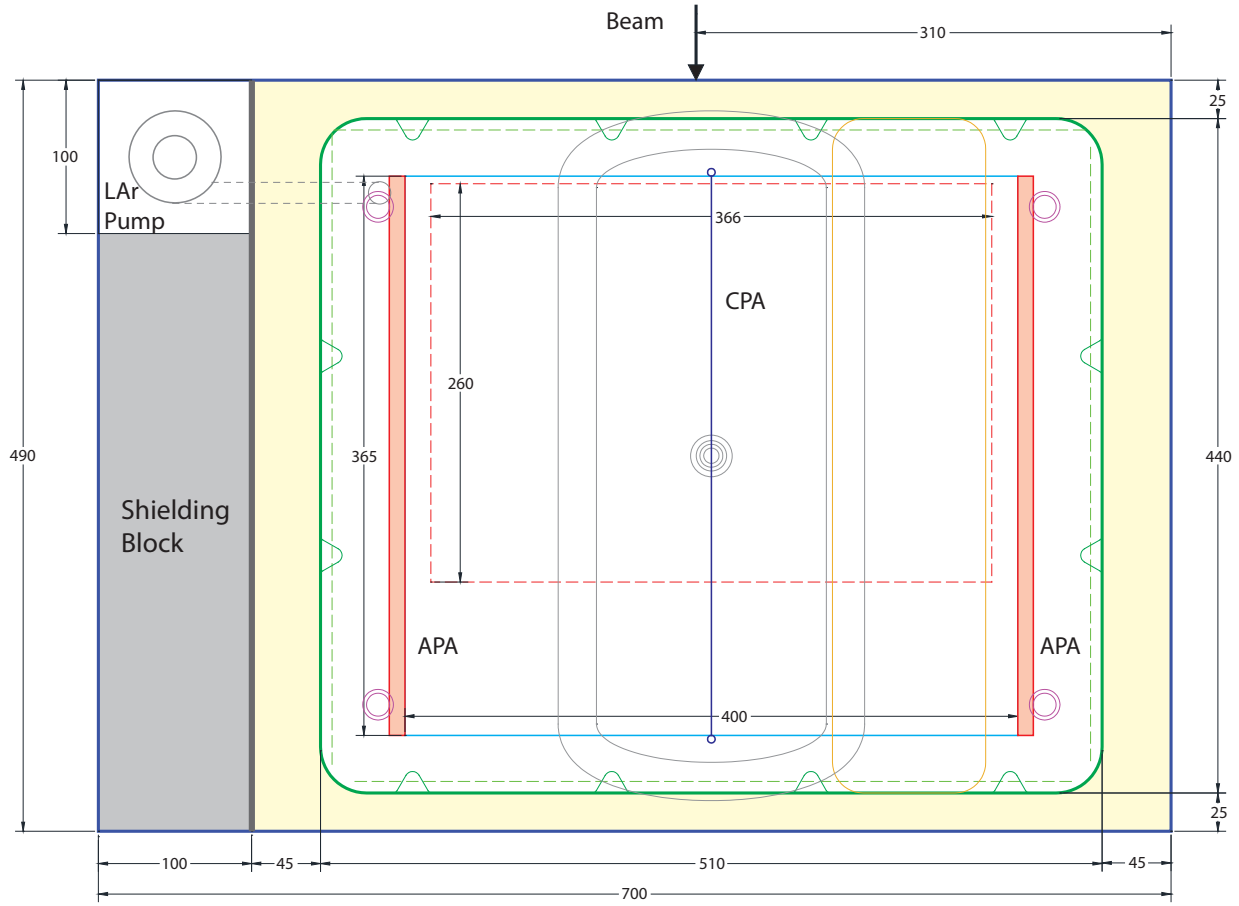

Figure 4.2: *Top view schematic drawing of the LAr1-ND detector concept. A membrane cryostat construction is built to fill the existing enclosure. Foam insulation surrounds the corrugated stainless steel membrane, with a thickness of 25 cm on the bottom, 40 cm on top, 45 cm to the beam left and right and 20 cm at the upstream and downstream ends. The neutrino beam enters from the top in this graphic. In this figure and the next, blue lines represent the pit, green solid the membrane flat surface, green dashed the membrane corrugations, yellow the TPC installation hatch, white the membrane knuckles, cyan the active volume, and red dashed the fidicual volume.*

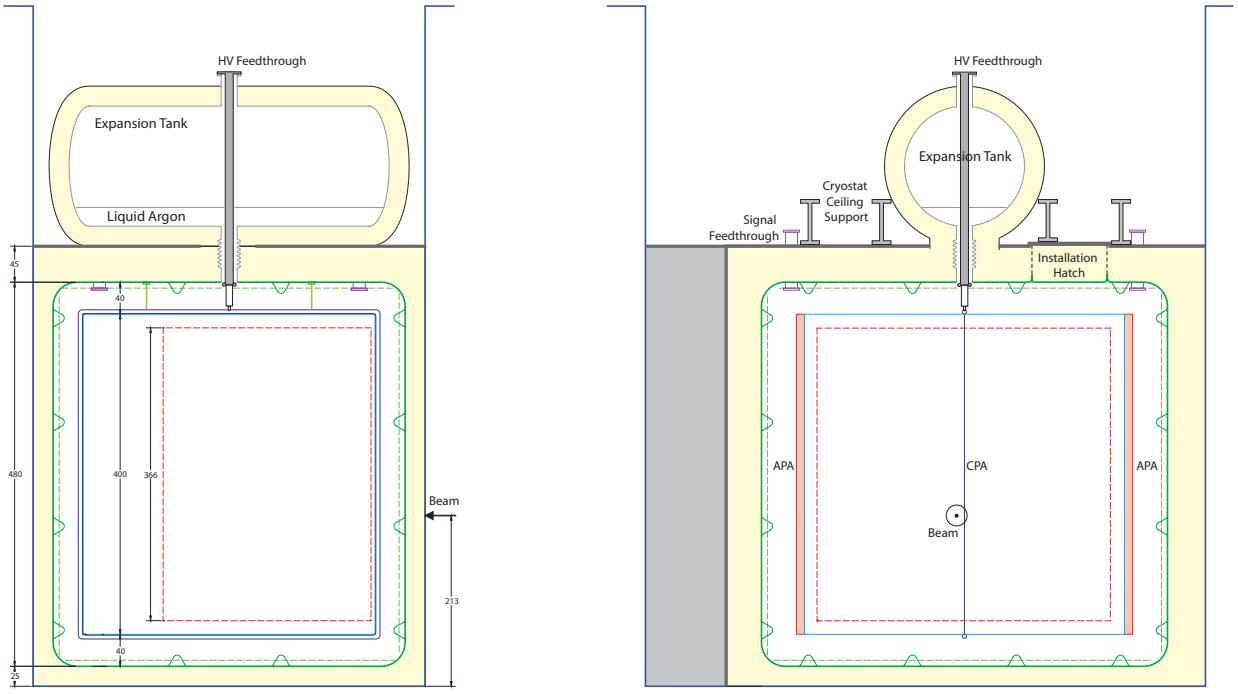

Figure 4.3: *Side view schematic drawings of the LAr1-ND detector concept. The "expansion" tank, which contains the argon gas pressure buffer for the cryostat, and the signal feedthroughs are shown at the top.*

4.2.1 Membrane Cryostat

The conceptual design for the LAr1-ND cryostat is a rectangular vessel constructed with an industrial membrane cryostat technology extensively used for shipping Liquid Natural Gas (LNG) and for storage of LNG above ground and in caverns. Depending on the vendor, a membrane tank uses a 1.2–2 mm thick stainless-steel primary liner to contain the liquid cryogen. The membrane cryostat relies on external support from a surrounding cavern or a reinforced concrete structure to support the hydrostatic load of the contents, again making the existing enclosure an ideal location for this detector. The commercially engineered membrane system consists of the following sequence of layers, from innermost to outermost: the stainless-steel primary membrane; a layer of polyurethane foam insulation; a thin fiberglass-aluminum secondary membrane that contains the LAr in case of any leaks in the primary membrane; another layer of insulation; a barrier to prevent water-vapor ingress and the concrete support structure (See Figure 4.4).

This in-ground tank arrangement (ie. offering access only from the top) makes optimum use of the excavated pit in which it is installed and minimizes safety concerns. The roof of the cryostat is constructed of truss-reinforced steel plate covered on the cryostat side with

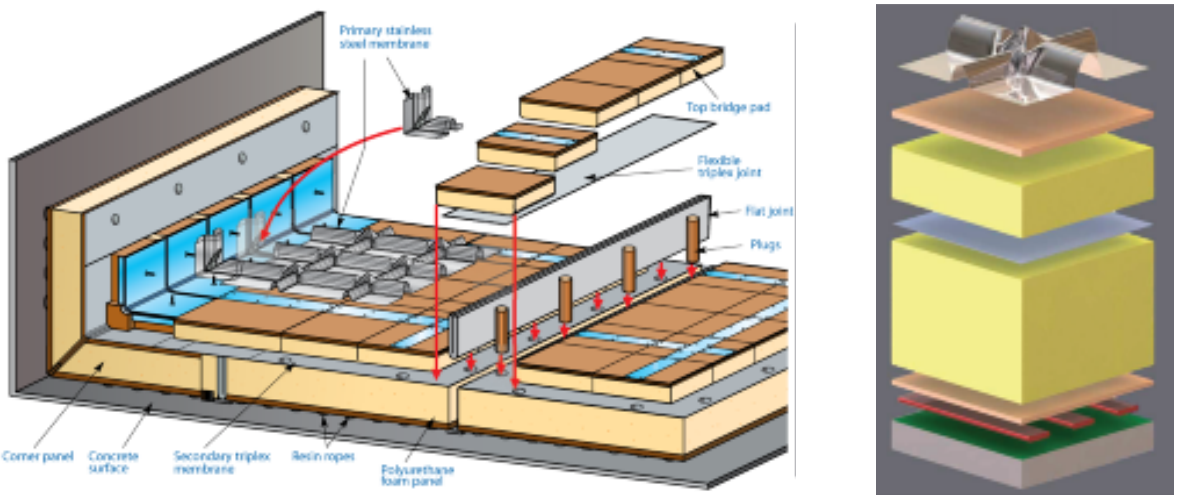

Figure 4.4: *Cross Sectional view of the layers that comprise a Membrane Cryostat. Courtesy of Gaz Transport & Technigaz.*

the insulated membrane system. All cryostat penetrations will be made through the roof. Relay racks containing the DAQ components will be located directly above each cryostat signal feedthrough.

The membrane cryostat is a robust design with a proven record spanning more than 1600 tank-years of service, predictable cost, and known installation time. Figure 4.5 shows a photo of the 35 ton membrane cryostat prototype that has been constructed at Fermilab, using similar technology. This test is to verify this technology for use in detectors of this scale and is the intended technology for use in LBNE.

LAr TPCs that have operated to date have achieved good argon purity after vacuum pumping the cryostat prior to filling with LAr. Vacuum pumping is an effective means of removing oxygen and water from materials within the cryostat but membrane cryostats are not normally designed to be evacuated. However, purging with purified argon gas has been found to be equally effective. The purging approach has been verified in the Liquid Argon Purity Demonstrator (LAPD [25]) and is the procedure that will be used for the initial fill of MicroBooNE.

In order to achieve an electron mean free path greater than the design drift distance of 2 m, the commercial liquid argon with which the cryostat will be filled must be purified to remove electronegative contaminants (principally water and oxygen) to a concentration well below parts per billion. This will be done by recirculating the liquid argon through commercial molecular sieves and oxygen scrubbers. Once the desired purity is achieved, the only sources of contamination are leaks and outgassing of materials in the warm gas above the liquid. Leaks must be avoided by design and testing of components of the final system.

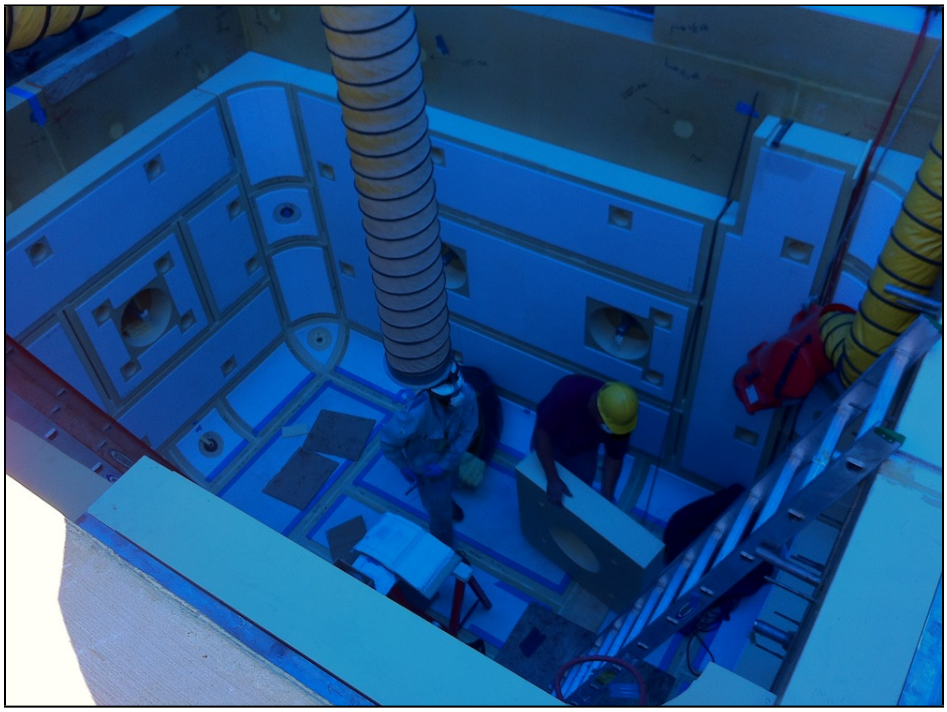

Figure 4.5: *The interior of the 35 ton prototype membrane cryostat under construction at Fermilab.*

In the liquid at 89K, the outgassing rates are so low that negligible amounts of oxygen and water enter the liquid. The cryostat is designed so that the bulk of the cryostat surface is wetted with liquid. Only a small volume of gas is contained in an insulated expansion tank above the cryostat. The walls and contents of the volume will be close to 89K minimizing outgassing. In addition, the contact area between the gas and liquid is small reducing the rate of injection of contaminants into the liquid. This gas ullage volume, which is necessary to maintain pressure stability in the cryostat, will be purified by a gas recirculation system through molecular sieves and oxygen getters. This small gas recirculation system should be sufficient to maintain the purity, without any liquid recirculation, during operation.

A potential problem in operating large LAr TPCs at the surface is the dynamic generation of space charge by cosmic ray ionization of the LAr. Positive ions drift very slowly in LAr compared to electrons, and the resulting space charge contained in the TPC at any time will create an electric field that distorts the ideal straight electron drift to the anode that enables TPC operation. Statistical fluctuations in the distribution of the ionization and flow of the liquid (which occurs at velocities comparable to the positive ion drift) will make these distortions time dependent, and therefore very difficult to remove completely by calibration. To minimize this problem, we will install cooling panels, with pressurized LN_2 channels, along the walls, floor, and ceiling of the cryostat to minimize convective flow of the LAr caused

by the thermal load of the (imperfectly) insulated walls. This will remove a large part of the time dependence of the space charge distortions. Furthermore, we plan to install and operate an UV-laser system similar to that of the MicroBooNE experiment for the accurate calibration of the TPC.

A further advantage of the inclusion of an expansion tank and cooling panels is that the liquid argon in the active volume will be removed from the saturation point. This will inhibit bubble formation, which is a potential source of breakdown in high field regions. This will make the drift high voltage system more reliable.

4.2.2 Cryogenic System

The choice of the cryogenic systems layout and location is intended to optimize safety and efficiency. It will:

- Minimize the risk of personnel injury to any Oxygen Deficiency Hazard (ODH)
- Minimize heat ingress to the cryogenic system (by minimizing piping length and pump power)
- Minimize the volume of the argon system external to the cryostat and hence minimize the potential for argon escape or contamination
- Provide safe access to refrigeration equipment that requires periodic maintenance

The LN_2 cooling system, argon re-condensers, and gas/liquid purifiers will be located in a surface building immediately adjacent to the cryostat pit. The surface facility will include a LAr and LN_2 receiving dewars. The cryostat will hold an inventory of $\sim$155 tons of liquid argon. The liquid argon purification system will be required only to achieve the initial liquid argon purity. After that the circulation of the argon gas in the expansion tank will maintain the high purity. The purification plant will consist of duty and standby molecular-sieve columns to remove water and an activated copper column to remove oxygen.

4.2.3 Time Projection Chamber

The Time Projection Chamber (TPC) subsystem consists of three types of mechanical components defining the electric drift field - anode plane assemblies (APAs), cathode plane assembly (CPA), and field cage assemblies (FCAs) - and all the in-vessel electronics, signal and power cables, their feedthroughs, as well as the low-and high-voltage power supplies for the electronics.

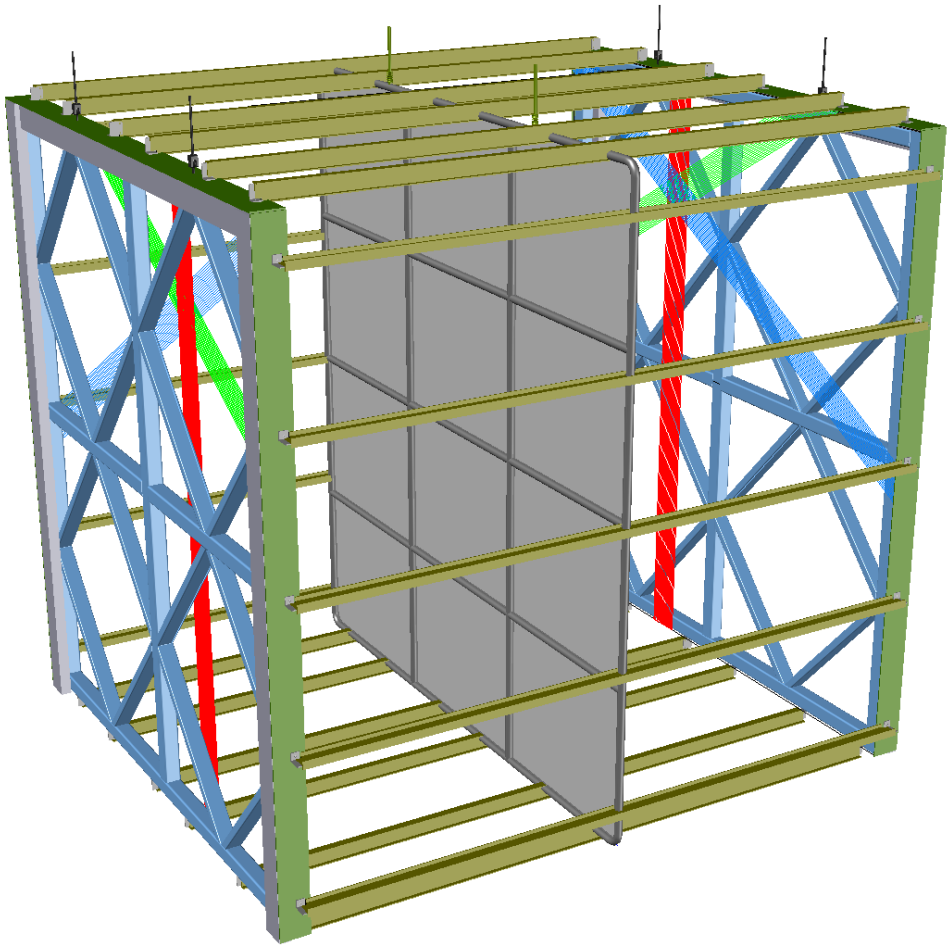

Figure 4.6: *Conceptual design of the LAr1-ND TPC. The FR4 field cage panels are removed from view.*

Overview

The TPC is located inside the cryostat vessel, completely submerged in liquid argon at 89K. The entire TPC structure is suspended under the cryostat roof via integrated attachment points. All cables (power and signal) from the cold electronics are routed through four feedthrough ports on the top of the cryostat to the DAQ system. The TPC (Fig. 4.6) consists of two APAs near the beam left and right walls of the cryostat. The active area of the APAs is 3.65 m wide and 4 m tall. The CPA is centered between the two APAs. The open sides between each APA and the CPA are surrounded by 4 FCA modules, constructed from FR4 printed circuit panels with parallel copper strips to create a uniform drift field. The drift distance between each APA and the CPA is 2 m. The active LAr mass in the TPC is 82 tons.

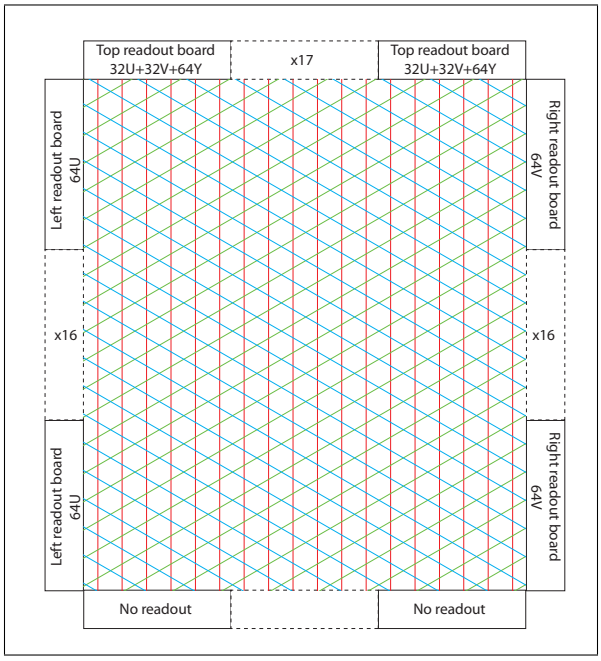

Figure 4.7: *Schematic drawing of the wire arrangement on each APA.*

Each anode-plane assembly holds three planes of wires. The wire pitch and angles are identical to that of MicroBooNE: 3 mm between wires and 3 mm between wire planes. Two induction planes (U & V) are at $\pm 60°$ from vertical, while the collection plane wires are vertical. Each wire is connected to a front-end readout channel. The wire readout arrangement is also identical to MicroBooNE, with banks of cold electronics boards at the top and two vertical sides of each APA (Fig. 4.7.) The total number of readout channels is 4736 per APA, 9472 in the entire detector.

The APA uses the same wire bonding method developed for the LBNE APAs, but without the continuous helical wrapping to avoid the ambiguity in track reconstruction. The design of the APA in principle allows tiling of APAs on all four edges with minimal dead space between modules. Placing the APAs close to the cryostat wall allows significant reduction in the unused LAr in the cryostat. This single sided APA concept may be applied to LBNE or other future LAr TPCs.

The electronic readout chain is implemented as CMOS ASICs designed for operation in LAr, and commercial FPGAs tested for cryogenic operation. The analog front end ASIC has 16 channels of preamp, shaper and driver circuits. The ADC ASIC utilizes a mixed-signal design, it has 16 channels of ADC with built in FIFO as shared buffer, followed by a first stage multiplexer with programmable multiplexing factor. The output of ADC is serialized with LVDS (low-voltage differential signaling), which is suitable for interface to

FPGA directly. Eight analog FE chips, eight ADC chips and one FPGA are mounted on a single readout board, instrumenting 128 wires. The FPGA provides the second stage of multiplexing, ASICs control and monitoring, and certain processing algorithms can also be implemented for data reduction. The FPGA further increases the multiplexing factor to 128:2, resulting in dual output channels for each of the 20 readout boards mounted on a single APA. Data from each of these output channels will be transmitted by a ∼2Gbit/s high speed serial link through a feedthrough at the top of the cryostat.

We plan for two cable bundles per APA, consisting of wires for low-voltage power, wire bias voltages, data out, clock in, and digital control IO, to connect to the outside of the cryostat. There will be four signal feedthroughs near the four corners of the cryostat roof.

Anode Plane Assemblies (APAs)

The anode plane assemblies (APAs) are 3.65 m wide, 4 m high and ∼20 cm thick. Each APA is constructed from a framework of stainless-steel tubes, with 3 layers of wires stretched over one side of the frame. Experiences from prior R&D has shown that a CuBe wire under tension can be reliably bonded to a copper-clad FR4 surface by a combination of solder (electrical connection) and epoxy (mechanical bonding). This bonding technique greatly simplifies the electrical connection to the readout electronics, and can be easily automated with commercial equipment. At 150 micrometers diameter, the break tension of a hardened CuBe wire is about 30 N. To ensure no wire breakage in the TPC, the nominal operating tension of the wire will be set to under 10 N. The final wire tension and the need for intermediate wire support will be determined by further engineering studies.

The three wire planes will be electrically biased so that electrons from an ionizing-particle track completely drift past the first two induction planes (U & V), and are collected by the final plane (Y). Since the wire pitch and wire plane spacing of this APA is identical to that of MicroBooNE, the bias voltages for the electron transparency condition should also be the same: $V_U \sim -200$ V, $V_V = 0$ V, and $V_Y \sim 440$ V with a drift field of 500 V/cm.

To maintain a 128 channel modularity on the FEE boards on the top edge of the APA, the FEE board must be 192 mm long (32U, 32V, 64Y). In the vertical direction, 128 channels of U or V wires span 443 mm. Over this distance, the differential CTE between FR4 and stainless steel in LAr becomes large enough to stress connectors. To reduce the risk of broken contacts, the vertical boards are grouped as 64 wire modules (222 mm). The current APA uses 19 horizontal boards to form the 3.65 m active width, and 18 vertical boards (@222 mm each) to form the 4.0 m active height.

At a nominal wire tension of 5 N, the full set of wires exert a force of $\sim$ 2500 N/m on each edge of the APA. The wire frame must be able to withstand the wire tension with a minimal

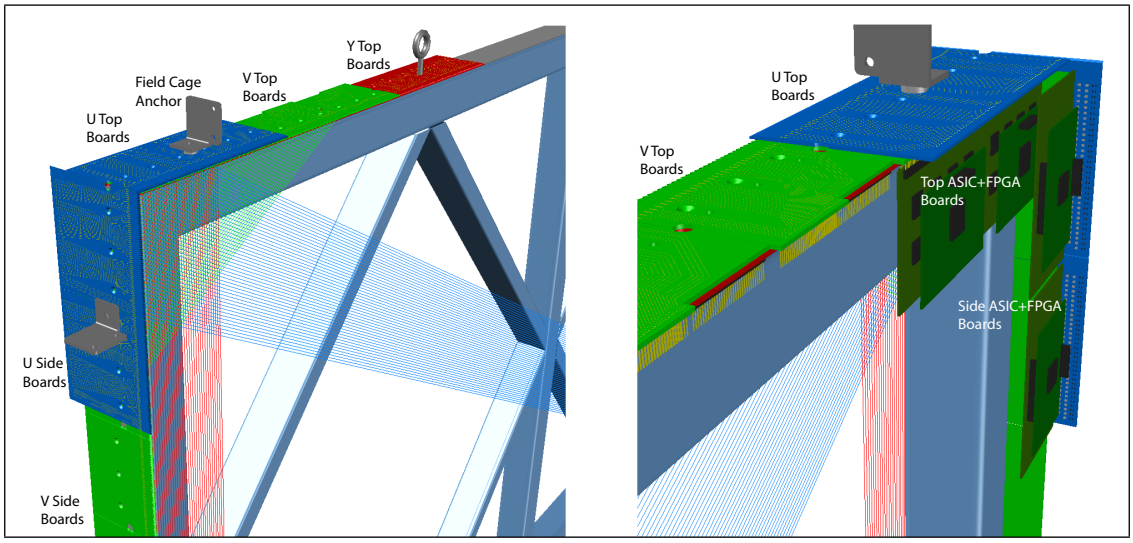

Figure 4.8: *Corner view of an APA. Wires strung at* 0^o, $\pm 60^o$ *are attached to wire bonding boards at the sides and ends of the APA. One readout board is shown in dark green.*

distortion and no buckling. A conceptual design of the wire frame is shown in Fig. 4.8. Finite element analysis will be performed to ensure the deflection of the frame under full wire tension does not exceed 0.5 mm, while minimizing the weight of the structure.

Figure 4.9 shows two major cross sections of an APA. The left figure is the cross section of the top edge of the APA. The three planes of wires are attached to their respective wire-bonding boards through a combination of epoxy and solder. Precision curved grooves are machined onto the leading edges of the boards to guide the wires into the correct position, and to prevent sharp kinks from forming on the wires. Copper traces on a wire bonding board connect each of the readout wires to the corresponding pins on the opposite end of the board. An array of mating connectors on the front-end readout boards is plugged onto the stack of wire bonding boards, making electrical connection between the readout electronics and the sensing wires. A FPGA daughter card is plugged into each FEE board to multiplex the 128 channels into a few output cables. At the bottom edge of the APA, the three planes of wires are simply fixed mechanically onto a set of narrower wire bonding boards. The right figure shows the cross section of one vertical edge of the APA. Only the U & V wires cross this edge. And among these two planes, only one of them needs to be read out (the other plane is read out on the other vertical edge of the APA). The location of the electronics boards are moved further back to clear the readout boards behind the top edge of the APA. A U shaped sheet metal channel serves as both a bubble deflector and a cable strain relieve structure. Protective guards will be placed on all four edges of an APA during storage and handling. With this design, one can tile an arbitrarily large sensing area with only centimeter scale dead gaps.

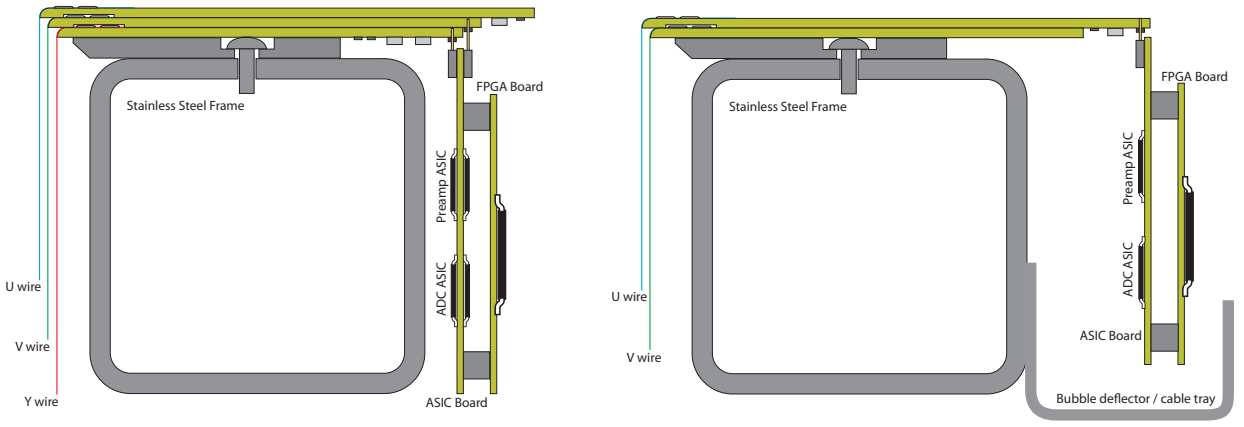

Figure 4.9: *Illustration of two major cross sections of an APA frame. Left: top horizontal edge; Right: a vertical edge.*

Cathode Plane Assembly (CPA)

The cathode plane assembly (CPA) has the same dimensions as the APAs. It is made of a stainless-steel framework, with an array of stainless-steel sheets mounted over the frame openings. The solid cathode surfaces can be replaced with transparent wire mesh if needed. At a 500 V/cm drift field and 2 m drift distance, the cathode plane needs to be biased at −100 kV. Mounting tabs for the FCA modules will be pre-installed on the outer edges of the CPA.

Field Cage Assemblies

Each pair of facing CPA and APA forms an electron-drift region. A field cage must completely surround the four open sides of this region to provide the necessary boundary conditions to ensure a uniform electric field within, unaffected by the presence of the cryostat walls. We propose to use copper-clad FR4 panels similar to those used in ArgoNeuT and planned for use in LBNE. Parallel copper strips will be etched or machined on the panels and will be biased at appropriate voltages by a resistive divider network. These strips will create a linear electric-potential gradient in the LAr, ensuring a uniform drift field in the TPC active volume. A FCA module is constructed from tiled FR4 sheets reinforced by several 2 m long fiberglass I-beams. Additional support structures are needed under the bottom FCAs such that two persons can stand on certain locations of the FCA during TPC installation.

TPC Assembly in the Cryostat

An installation hatch on the roof of the cryostat as shown in Figure 4.2 is needed to install the TPC. The installation sequence is envisioned to be the following:

- Install a raised floor over the corrugations on the cryostat floor.
- Lower the far end APA through the hatch onto a cart. Push the cart on the raised floor to the far end of the cryostat. Raise the APA and connect to the attachment points.
- Connect the cable bundles to the cold signal feedthroughs. Run DAQ to test the APA. Remove the raised floor on the far end.
- Lower the far end top and all 4 side FCAs into the cryostat. Connect the top FCA to the APA on one edge, suspend the other edge onto the ceiling. Secure all side FCAs to the side walls.
- Lower the CPA frame into the cryostat, and attach it to the ceiling anchor points. Install the HV feedthrough and check its contact to the CPA.
- Connect the top FCA to the CPA. Install the two side FCAs between the APA and CPA. Assemble and install the bottom FCA from components. Install cathode facing.
- Install the near end APA and connect the cables. Remove the remaining raised floor.
- Install the two side FCAs. Assemble and install the bottom FCA (some insulating support structure may be needed under the I-beams. They can be left under the FCA).
- Install the I-beams of the top FCA. Install the FR4 panels except one under the hatch. Exist the hatch. Install the last FR4 panel from above.
- Close and seal the hatch. Apply foam insulation on the hatch.

4.2.4 Readout Electronics and DAQ System

Readout Electronics

The LAr1-ND TPC will have two APA modules, each module has 4,736 channels, total 9,472 readout channels. The large number of readout channels required to instrument the LAr1-ND TPC motivates the use of CMOS ASICs for the electronics. Both analog FE ASIC

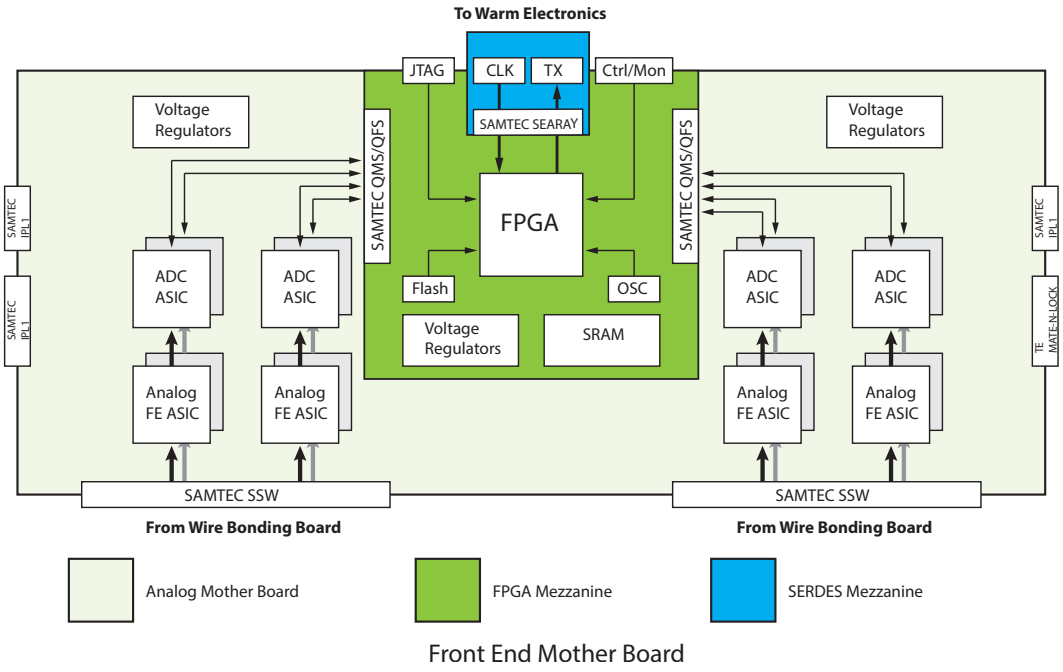

Figure 4.10: *Block diagram of Front End Mother Board*

and ADC ASIC, to a large extent, have already been developed for LBNE, and analog FE ASIC is being used in MicroBooNE. The entire front end electronics chain is immersed in the LAr and operates at 89 K to achieve optimum signal to noise ratio. It is composed of a 16-channel analog FE ASIC providing amplification and shaping, a 16-channel ADC ASIC implemented as a mixed-signal ASIC providing digitization, buffering and the first stage of multiplexing, a FPGA providing the second multiplexing stage, and voltage regulators. Eight analog FE ASICs, eight ADC ASICs plus a FPGA implementing multiplexer, clock, control and monitoring circuitry comprise a single 128-channel front end mother board. The FPGA on each motherboard will transmit data out of the cryostat on twinaxial copper pairs running at multiple Gbit/s through a feedthrough to the DAQ system, and receive programming instructions from the DAQ system.

Each APA will have 55 front end mother boards. 19 boards on top of TPC, each board has 128 channels. 18 boards on each side, each board has 64 channels. A block diagram of the 128-channel front end mother board is shown in Figure 4.10. Both analog FE ASIC and ADC ASIC have been designed and fabricated in a commercial CMOS process (0.18 um and 1.8 V). This guarantees a high stability of the operating point over a wide range of temperatures, from room temperature to 77 K. The ASICs are packaged in a commercial, fully encapsulated plastic QFP 80 package. Cold FPGA will interface to analog FE ASICs

and ADC ASICs on the front end mother board. It will control and monitor ASICs, and receive data from ADCs. Once data arrives at FPGA, a second stage multiplexer will be implemented to further reduce the number of data links to outside of the cryostat.

The design is to support transparent data readout without any compression over 2 Gbit/s serial links. An efficient zero-suppression scheme can be implemented in FPGA to greatly reduce the total data volume. Each mother board processes 128 detection channels, clock will come in through RX links while data is sent out over TX links. Voltage regulators used on board have been qualified in liquid nitrogen. On board SRAM is used to temporarily buffer events if a more sophisticated algorithm is used to process data. Commercial SRAM chips that works at cryogenic temperature has also been identified. The prototype front end mother board is being designed for the LBNE 35 ton prototype, the estimated power dissipation is $\sim$20 mW/channel.

DAQ System

The LAr1-ND TPC has 2 APAs, requires 110 front end mother boards, total 9,472 readout channels. The DAQ system will be located external to the cryostat vessel, with components in the detector hall and in an on-site control room. It consists of the "Warm Interface Module" (WIM), "Data Concentrator Modules "(DCM), timing system, network switch and computing farm. The data acquisition system is summarized in block diagram form in Figure 4.11. The design strives to minimize the impact of single-point failures, and maximize the use of commercial components.

WIM is installed on top of signal feed-through flange. It receives data from front end mother boards and sends data to downstream DAQ hardware. The WIM is the gateway between in-vessel electronics and downstream DAQ hardware. It will receive data from front end mother boards over high speed serial links. On board FPGA has computing power to do further data processing before sending data to downstream DCMs. By using FPGA with multiple ($>$ 48) high speed ($>$ 10 Gbit/s) embedded serializers, the WIM will aggregate data from in-vessel electronics, and greatly reduce the number of links to downstream DCM. Each WIM will serve either 19 128-ch front end mother boards or 36 64-ch front end mother boards on one APA, receive data from 38 serial links running at 2 Gbit/s. The output link will be running at 6.6 Gbit/s, 12 links are required to support full volume data transmission without any data reduction. The data transmission to DCM will be over high speed parallel fiber optical link. The whole system will need 4 WIMs for 9,472 readout channels. DCM is a commercial PCI Express Gen3 module, plugged in the PC that sits on the DAQ platform. It will receive data from WIM over high speed parallel optical links, and connect to the network and computing farm through a PC mainframe. The whole experiment will need four DCM

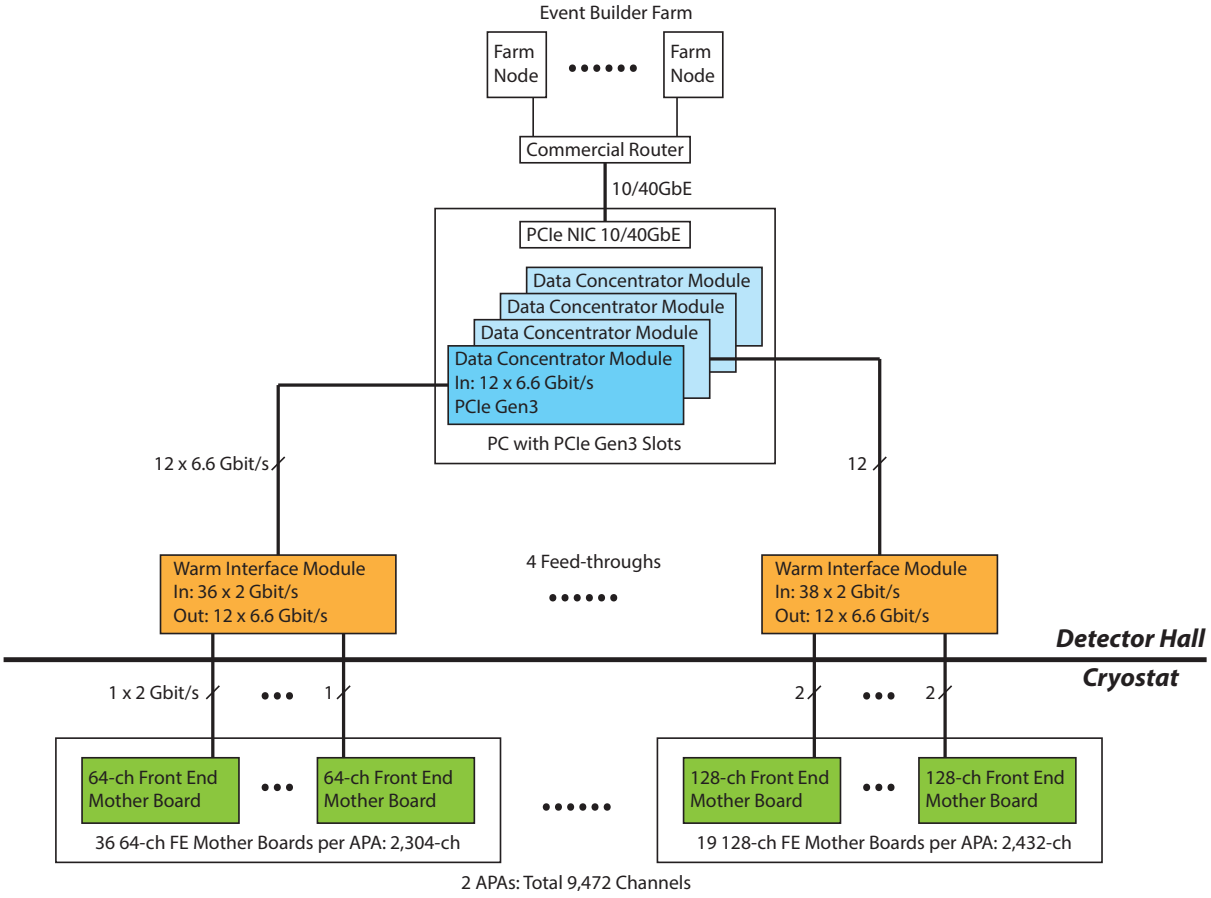

Figure 4.11: *DAQ block diagram*

modules. If a more sophisticated algorithm is required to process data before building events, more DCMs can be installed in the PC mainframe to expand the processing capability. The PC mainframe provides 10 GbE or 40 GbE interface to a local farm of commodity computers for event building over commercial network routers.

4.2.5 Trigger - Light Collection

Scintillation light is produced copiously in liquid argon at 128 nm. Detection of this light plays several important roles in LAr TPCs. For a surface detector in a beam, like LAr1-ND, the scintillation light provides a tag of events in-time with the beam pulse, allowing rejection of cosmic rays. The light also provides the T_0 for non-accelerator events (such as supernova events); for events not associated with a beam spill and no minimum ionizing particle for

calibration of drift-electron-loss, the T_0 from light collection is necessary for accurately reconstructing the event energy. Localization of event vertices using light collection reduces reconstruction time for TPC tracks. Lastly, ratios of late (1.6 μs time constant from the triplet state) to early (6 ns from the singlet state) light can allow for particle identification in events.

The traditional method for detecting the scintillation light uses tetraphenyl butadiene (TPB) coatings on photomultiplier tubes (PMTs) or plates placed in front of the PMTs. For example, in MicroBooNE the coating is applied to an acrylic plate positioned directly in front of an 8-inch R5912-mod PMT [26]. The large-PMT design is known to work well in modest-sized LAr TPCs. However in ultra-large detectors, where space is at a premium, a more compact system is desirable.

To address this problem a light-guide-based system for detecting scintillation light has been proposed for LBNE. The $0.6 \times 2.54 \times 51$ cm^3 coated acrylic bars are read out at the end using three SensL MicroFB-60035-SMT silicon photomultipliers (SiPMs), that each have a 6×6 mm^2 active area. The bars are arranged in a frame, providing a flat-profile light assembly that can be inserted into dead regions between LAr TPC wire planes.

The R&D program has proceed in three phases, briefly described below. The results show that, while more development is highly desirable, the system works properly and is proposed as the basic design for light collection in the LAr1-ND detector.

The initial phase of the bar studies [27] demonstrated the basic concept. The lightguides are constructed of a clear TPB-based coating with an index of refraction that was chosen to match acrylic bars. Acrylic was chosen as the substrate because it is resilient to cryogenic cycling. Visible light that is emitted when UV photons hit the TPB coating can suffer total internal reflection because the acrylic has an index of refraction for blue light ($n = 1.49$) that is higher than that of liquid argon ($n = 1.23$). In the initial version the light was guided to a PMT. The process of developing these guides, in concert with studies for light collection in MicroBooNE, led us to important results on degradation of TPB with light which must be addressed in any large-scale production [28, 29]

Phase 2 of the R&D program focussed on narrowing down design choices, especially related to four issues. The first was to narrow down the options for recipes on the TPB coatings, which must balance the choice of matrix material (e.g. polystyrene or acrylic) with the percentage of TPB that can be dissolved into the matrix while maintaining the clarity and smoothness of the surface. The second was the best method to apply the coating to the bars, recognizing that the technique must be industrialized for LAr1 and LBNE use. The third issue was to identify a vendor to supply UV transparent acrylic bars with a suitable attenuation length that are cryogenically sound. The tests have indicated that UV transparency also extends sensitivity in the violet, where TPB emits. The fourth issue was

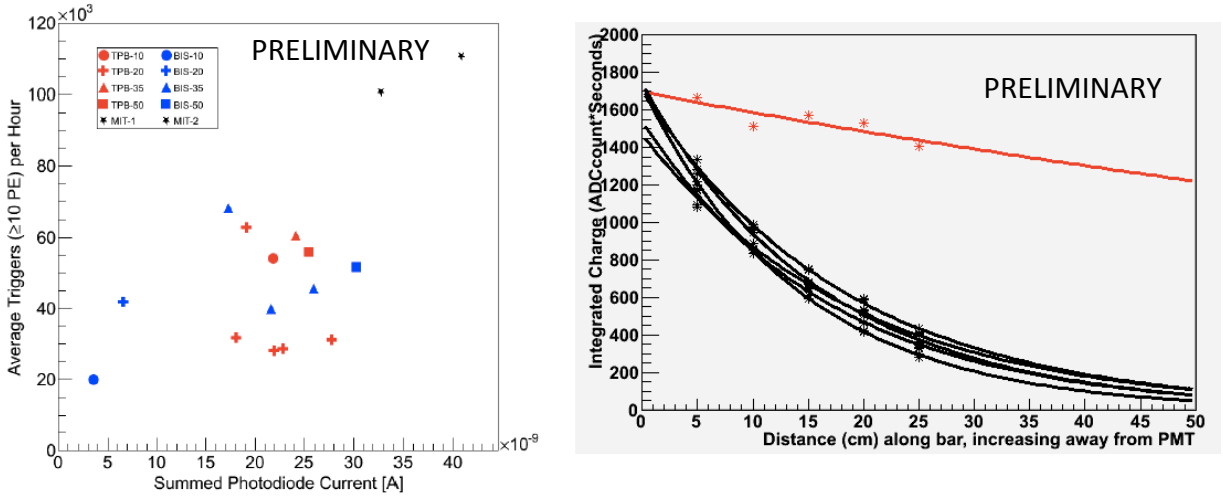

Figure 4.12: *Comparison of coatings and coating methods. Left: Response of various lightguides to cosmic rays in a run in the TallBo cryostat, with preferred recipe indicated by the black stars. Right: Attenuation length of non-UV acrylic bars coated with painted coating (black) compared to UV transparent acrylic bars dip-coated; preferred recipe for coating used in all cases. Results are preliminary.*

choosing the best readout method–PMTs versus SiPMs. Having made decisions on each issue, as described below, we now enter phase 3, where we work to optimize production.

Entering phase 3, the best choice of coating recipe consists of a 1:2 TPB:acrylic ratio, dissolved in 50 ml of toluene for every 1 g of acrylic, with a 1:5 ethyl alcohol:toluene ratio. The ethyl alcohol acts as a surfactant to smooth the coating [30]. Figure 4.12 (left), compares bars hand-coated using a brush with this recipe (black stars) to coatings (blue, red) that use a mechanical spray coating/heat-embedding method [31]. The data were taken in the TallBo cryostat at the Proton Assembly Building at FNAL, which can be evacuated before filling with high purity argon. The light source was cosmic ray muons tracked by a segmented hodoscope. Multiple figures of merit were devised in this analysis [32], and which we can use in the future. In the case of this figure, we use the number of pulses above a given threshold per hour versus the average summed SiPM current.

An important development was the choice of 6 mm thick UV transparent acrylic for the bars [30]. This, along with a new dip-coating method for applying the coating, has led to bars with very long attenuation length. Measurements using a 215 nm LED illuminating guides read out by a PMT [33] are shown in Figure 4.12 (right). While results are preliminary, the improvement is dramatic. UV transparent guides which are dip-coated will be run in the next iteration of TallBo studies, scheduled for February, 2014.

The SiPMs are clearly a better choice than PMTs because the quantum efficiency is higher and they run with 24 V providing a 10^6 gain. In the cryogenic liquid the noise level is low and individual peaks can be resolved up to more than 20 photoelectrons. The primary issue with the SiPMs, at present, is maintaining a good mechanical connection for the readout, given the stress of immersion in the cryogenic argon.

The phase 3 steps in the studies will include continuing improvements in coating and attenuation, although, at this point, these are expected to be incremental. In the February 2014 run, we are studying manipulation of the wavelength and late to early light ratio through introduction of xenon, using an injection system developed for nitrogen studies [34]. In the longer term, the primary emphases will be placed on 1) engineering, especially focusing on industrializing the coating and installation methods, and 2) extensive, long-term testing of the guides. We note that while the results of this work will be first applied to LAr1-ND, our efforts are directly valuable to LBNE and to the wider community interested in light collection in liquid argon.

Chapter 5

Experimental Sensitivity

By itself, the MicroBooNE experiment can confirm and determine the nature of the excess observed by MiniBooNE at the ∼500 m distance on the Booster Neutrino Beam (BNB), but it can not address the question of whether that excess appears over a distance or is intrinsic to the beam. Full interpretation of any anomalous excess, regardless of whether it is electrons or photons, will require a second detector at a near location that is equally sensitive to the same interactions. LAr1-ND can address this important issue. In the case that the excess is electron like, the sterile neutrino oscillation interpretation is of particular interest. For this particular scenario, a near detector extends the physics program in the BNB by also enabling a sensitive test of ν_μ disappearance through charged-current interactions, as well as a direct search for active flavor disappearance into sterile flavor through neutral-current channels. The classification of any excess as evidence of sterile neutrinos relies on the precise and multifaceted channels that can only be studied with a near detector like LAr1-ND.

In this Chapter we explore the physics potential of augmenting the existing MicroBooNE detector at 470 m with a smaller LAr TPC near detector housed in the existing (but empty) SciBooNE detector hall, located at 100 m on the BNB. This is the experiment we are proposing here. We present the sensitivity of several complementary approaches to testing existing anomalies or searching for evidence of high-Δm^2 neutrino oscillations.

The physics capabilities presented in this Proposal assume an exposure of 2.2×10^{20} protons on target (POT) for the LAr1-ND experiment in neutrino mode running of the BNB. It is envisioned that LAr1-ND will initially run in the final year of the approved run for MicroBooNE (6.6×10^{20} POT total), therefore requiring no additional running beyond that already planned to achieve the Phase-I goals.

Section 5.1 briefly describes the Monte Carlo simulation used to perform the sensitivity studies. In Sec. 5.2.1 we present the ability to confirm an excess of electron neutrinos that

matches exactly the anomalous excess reported by MiniBooNE. In Sec. 5.2.2 we focus on testing a $\nu_\mu \rightarrow \nu_e$ appearance scenario in the context of a 3+1 sterile neutrino model as was reported by LSND. Section 5.2.3 shows the reach of a two detector configuration in searching for ν_μ disappearance, a far less model-dependent test of $\nu_\mu \rightarrow \nu_x$ oscillations. A similarly important test of active to sterile oscillations can be performed using neutral-current interactions for which the sensitivity is described in Sec. 5.2.4. In Sec. 5.2.5 we discuss the ability to measure the cross section for single photon production should the low-energy excess be found to be photons instead of electrons. Finally, Sec. 5.2.6 gives the expected event rates for different types of interactions, indicating the ability to make precise neutrino-argon cross section measurements in LAr1-ND. Moreover, Appendix A describes the possibility of dark matter searches with this detector in the future with Booster Beam off-target running and Appendix B briefly outlines the physics reach of a possible future extension to this experimental program. The addition of a 1 kton-scale far detector located at 700 m, LAr1-FD, would provide a powerful opportunity to understand the anti-neutrino mode anomalies and potentially make precision measurements of oscillations to sterile states in neutrino mode.

5.1 Monte Carlo Simulation

To estimate physics sensitivities of the experiment, a full Monte Carlo simulation is used. The process begins with a beam simulation, verified against the MiniBooNE beam Monte Carlo, which estimates the Booster Neutrino Beam flux produced in the target hall. The flux is then propagated using a dedicated software package (GSimple) to the detectors at 100 m and 470 m, as well as 700 m. The neutrino interactions themselves are simulated using the GENIE neutrino event generator [35] (v2.8.0). GENIE includes models for all relevant neutrino-nucleon cross sections and final state interactions.

Particles exiting a nucleus after the neutrino interaction are passed on to the LArSoft framework [36], which uses Geant4 [37] to simulate the electromagnetic and hadronic interactions within the liquid argon detector volumes. Geometry descriptions, specified using the GDML markup language, are provided for each detector studied.

We do not apply full reconstruction in the LArSoft framework, instead we base our assumed efficiencies off of studies using the Reconstruction Tools in the LArSoft framework. For example we estimate a 94% rejection rate of single photon background coming from π^0 decays or other sources using the dE/dx tag in the first few centimeters of the electromagnetic shower. This value is based on running the current LArSoft reconstruction chain on single photon and electron events and requiring 95% purity of the electron sample.

To simulate calorimetric energy reconstruction, the incoming neutrino energy in each Monte Carlo charged-current (CC) event is estimated by summing the energy of the lepton and all charged hadronic particles above observation thresholds present in the final state. This approach is used in the analysis of both ν_e and ν_μ charged-current events described next. It should be noted that this method is one possible approach to estimating the neutrino energy. The liquid argon TPC technology enables a full calorimetric reconstruction, but other methods can be used as well, such as isolating charged-current quasi-elastic (CC QE) events and assuming QE kinematics. The ability to apply complementary approaches to event identification and energy reconstruction will provide valuable cross checks of the measurements performed.

The advantage of performing the full simulation of the neutrino events in an oscillation free model, is that we can accurately model realistic backgrounds for the multiple channels in which we are sensitive to sterile neutrino signals instead of assuming, e.g. flat distributions. The specific backgrounds will be described in more detail in the next sections.

5.2 Analysis of Booster Beam Events

In Sec. 5.2.1 we set out to estimate the ability of LAr1-ND to test the nature of the MiniBooNE neutrino anomaly in a way independent of any specific oscillation model. The approach taken in this study does not use a full Monte Carlo simulation (though it does rely on MC studies for efficiencies), but the procedure is easy to follow and it is informative to see directly how the technology impacts aspects of the measurement. In later sections (5.2.2–5.2.4) we use instead the full simulation to assess sensitivities to ν_e appearance, ν_μ disappearance and active to sterile oscillations with neutral-current (NC) events with LAr1-ND.

5.2.1 Sensitivity to MiniBooNE Low-Energy ν_e Excess

With this analysis, we are addressing the straightforward question: *Does the anomalous excess of electromagnetic events reported by MiniBooNE, whether electrons or photons, appear over a distance or exist intrinsically in the beam?* To answer this we need to make a measurement at a near location in the beam that has good sensitivity to a MiniBooNE-like excess. We will show, therefore, the significance with which LAr1-ND would observe an event excess of the same size as that reported by MiniBooNE.

Starting from the event distribution in the left panel of Fig. 2.2 and reported in [11], we directly scale (up or down) the exact event rates observed by MiniBooNE, accounting for anticipated differences in event selection efficiencies due to the LAr TPC technology as well

as fiducial masses, beam exposures and detector locations.

Tables 5.1 and 5.2 illustrate this exercise for the LAr1-ND and MicroBooNE detectors. The ν_e charged-current quasi-elastic selection efficiency in MiniBooNE was 30–40%, and we assume a factor 2 increase with LAr TPC detectors. Neutral-current events with single photons in the final state represent an irreducible background in MiniBooNE since photons look identical to electrons in a Cherenkov detector, but in a LAr TPC we estimate a 94% rejection rate using the dE/dx tag in the first few centimeters of the electromagnetic shower (see Sec. 5.1).

We also scale for differences in detector mass and beam exposure. For MicroBooNE we assume a 61.4 ton fiducial mass and the approved 6.6×10^{20} protons on target (POT). These are to be compared to the 450 ton fiducial mass of the MiniBooNE detector and the 6.46×10^{20} POT exposure of the final MiniBooNE neutrino mode sample. Also, the MiniBooNE detector was located 541 m from the BNB target while the MicroBooNE detector is a little closer at 470 m. Simulation confirms that the flux falls off as $1/r^2$ between these two positions. This gives us the following relative scale factors for electron and single photon final states in MicroBooNE relative to MiniBooNE:

$$\begin{aligned} f^e_{\mu B} &= 2 \times (61.4/450) \times (541^2/470^2) \times (6.6/6.46) = 0.369 \\ f^\gamma_{\mu B} &= (0.06/0.30) \times (61.4/450) \times (541^2/470^2) \times (6.6/6.46) = 0.037 \end{aligned} \tag{5.1}$$

For LAr1-ND, these scale factors are reduced for the smaller fiducial mass (49 ton) and shorter exposure. We assume one year of concurrent running with MicroBooNE, or 2.2×10^{20} POT. The neutrino flux, however, is higher at the 100 m location compared to the MicroBooNE location at 470 m. Figure 3.3 shows the LAr1-ND/MicroBooNE flux ratio as a function of neutrino energy according to the beam simulation. For neutrino energies below ∼1 GeV, there is about 30× more flux in the near detector. We use this factor 30 to estimate the number of events in LAr1-ND by scaling from our estimates for MicroBooNE:

$$\begin{aligned} f^e_{ND} &= f^e_{\mu B} \times (49/61.4) \times (2.2/6.6) \times 30 = 2.95 \\ f^\gamma_{ND} &= f^\gamma_{\mu B} \times (49/61.4) \times (2.2/6.6) \times 30 = 0.29 \end{aligned} \tag{5.2}$$

In Table 5.1 we estimate the number of events in nine different background categories by scaling from the MiniBooNE neutrino mode results in the energy region below 475 MeV. Backgrounds include both intrinsic sources of ν_e as well as single photon final state ν_μ interactions. We also scale the excess event counts reported by MiniBooNE *as if they are electrons* and we refer to this as the "Excess" or the "Signal". We estimate 49 background events and 47 signal events in MicroBooNE. In LAr1-ND we expect 380 signal events on top of 395 intrinsic ν_e and single photon background events.

Process	200 - 300 MeV (mB)	300 - 475 MeV (mB)	Total (mB)	Scaling (μB)	Total (μB)	Scaling (LAr1-ND)	Total (LAr1-ND)
Background from intrinsic ν_e							
$\mu \to \nu_e$	13.6	44.5	58.1	.369	21.5	2.95	171.3
$K^+ \to \nu_e$	3.6	13.8	17.4	.369	6.4	2.95	51.3
$K^0 \to \nu_e$	1.6	3.4	5.0	.369	1.8	2.95	14.7
Background from ν_μ misidentification							
ν_μ CC	9.0	17.4	26.4	.185	4.9	1.47	38.9
$\nu_\mu e \to \nu_\mu e$	6.1	4.3	10.4	.369	3.8	2.95	30.7
NC π^0	103.5	77.8	181.3	.037	6.7	0.29	53.4
Dirt	11.5	12.3	23.5	.037	0.9	0.29	6.9
$\Delta \to N\gamma$	19.5	47.5	67.0	.037	2.5	0.29	19.8
Other	18.4	7.3	25.7	.037	0.9	0.29	7.6
Background	187	228	415		**49.4**		**394.6**
Excess	45.2	83.7	128.9	.369	**47.6**	2.95	**380.0**

Table 5.1: *Estimated event rates in MicroBooNE and LAr1-ND with reconstructed neutrino energy 200-475 MeV determined by scaling from MiniBooNE event rates [11] and accounting for differences in fiducial masses, beam exposures and selection efficiencies between the detector technologies (see text).*

To estimate the significance of a MiniBooNE-like signal in LAr1-ND, we apply the fractional systematic uncertainties reported by MiniBooNE. We include an additional 10% uncertainty on the efficiency of the dE/dx cut applied to separate e/γ final states in a LAr TPC. The results of this analysis are shown in Table 5.2. We find that the 380 signal events expected correspond to a 6.8σ excess over the expected background of $395 \pm 19.9(\text{stat}) \pm 52.2(\text{syst})$, demonstrating that LAr1-ND can verify a MiniBooNE-like excess at 100 m with high significance in a very short time.

Several things are worth noting about this analysis. First, the MiniBooNE analysis selected charged-current quasi-elastic events in order to be able to make a reasonable estimate of the neutrino energy in the event by assuming quasi-elastic kinematics in the interaction. This scaling procedure would, therefore, correspond to only utilizing the ν_e CCQE interactions in LAr1-ND. In a tracking calorimeter detector like a LAr TPC it is possible to use the inclusive charged-current event sample, thus increasing further the signal to background ratio in the case of an excess of ν_e events. The analysis presented in this section is conservative in that it only scales the quasi-elastic event rate reported by MiniBooNE. Second, because this analysis does not use a full Monte Carlo simulation, it captures the general features of the expected event rates and their uncertainties but important details such as the difference

Process	Events (μB)	Events (LAr1-ND)	MiniBooNE unc.	dE/dx unc.	Total unc.	Error (μB)	Error (LAr1-ND)
$\mu \to \nu_e$	21.5	171.3	0.26	0.1	0.28	6.0	47.7
$K^+ \to \nu_e$	6.4	51.3	0.22	0.1	0.24	1.55	12.4
$K^0 \to \nu_e$	1.8	14.7	0.38	0.1	0.39	0.73	5.79
ν_μ CC	4.9	38.9	0.26	0.0	0.26	1.27	10.1
$\nu_\mu e \to \nu_\mu e$	3.8	30.7	0.25	0.1	0.27	1.03	8.26
NC π^0	6.7	53.4	0.13	0.1	0.16	1.10	8.77
Dirt	0.9	6.9	0.16	0.1	0.19	0.16	1.31
$\Delta \to N\gamma$	2.5	19.8	0.14	0.1	0.17	0.43	3.40
Other	0.9	7.6	0.25	0.1	0.27	0.26	2.04
Total	49.4	322.1				6.55	52.23

	MicroBooNE	LAr1-ND
Total Events	97	775
"Low-energy Excess"	47.6	380
Background	49.4	394.6
Statistical Error	7.0	19.9
Systematic Error	6.6	52.2
Total Error	9.6	55.9
Statistical Significance of Excess	6.8 σ	19.1 σ
Total Significance of Excess	**5.0** σ	**6.8** σ

Table 5.2: *Anticipated event rate and errors in MicroBooNE and LAr1-ND with reconstructed neutrino energy 200-475 MeV determined by scaling from the observed events at MiniBooNE [11]. Estimated significance to the MiniBooNE "low-energy anomaly" at each location is determined by assuming the MiniBooNE excess is not dependent on the neutrino propagation length.*

in detector volume shapes, target material or the differences between neutrino interactions on carbon vs. argon are ignored. Nonetheless, the exercise is valuable for estimating the experiment's sensitivity to the exact anomalous event excess reported by MiniBooNE, an important aspect of the physics program of LAr1-ND. In the following sections we will turn to utilizing a full simulation to assess the sensitivity to various searches for oscillations with the combination of LAr1-ND and MicroBooNE.

5.2.2 $\nu_\mu \to \nu_e$ Appearance

In this section we present the sensitivity of an experimental search for sterile neutrinos in the context of a 3 active + 1 sterile neutrino model (3+1). The signal is taken to be the

appearance of electron neutrinos through $\nu_\mu \to \nu_e$ transitions according to the two neutrino oscillation probability formula

$$P^{3+1}_{\nu_\mu \to \nu_e} = \sin^2 2\theta_{\mu e} \sin^2 \frac{\Delta m^2_{41} L}{4E} \tag{5.3}$$

where Δm^2_{41} is the mass splitting between the known mass states and a new state with $\Delta m^2_{41} >> \Delta m^2_{31}$. $\mathrm{Sin}^2 2\theta_{\mu e}$ is an effective mixing amplitude that combines the amount of mixing of ν_μ and ν_e with mass state ν_4

$$\sin^2 2\theta_{\mu e} \equiv 4|U_{\mu 4}|^2 |U_{e4}|^2 \tag{5.4}$$

To assess the sensitivity to appearance signals, we calculate a simple χ^2 between the expected background events and the total event rate predicted for combinations of oscillation parameters Δm^2_{41} and $\sin^2 2\theta_{\mu e}$.

The observed ν_e candidate event rate in LAr1-ND at 100 m is used to predict the expected rate (in the absence of oscillations) in MicroBooNE at 470 m. A near detector of the same technology allows cancelations of systematic uncertainties associated with electron identification efficiencies, background mis-identification rates, neutrino fluxes and neutrino-nucleus cross sections. The lower limit in the systematic uncertainties on the far detector background prediction is determined by the statistical power of the near detector sample, so a large ND sample is important.

To estimate the total event rates of electron neutrino events we consider the ν_e charged-current (CC) events and the different possible background events. We apply the following selections to the full Monte Carlo simulation of events in both detectors:

- **ν_e CC :** Electron neutrino charged-current interactions occurring within the fiducial volume are accepted with an 80% identification efficiency.
- **NC π^0 production :** Neutral-current interactions with any number of π^0 in the final state are considered as possible background events. If more than one photon converts within the fiducial volume, the event is not considered as background. For events where only one photon converts within the fiducial volume, a 94% photon rejection rate is applied (corresponding to the expected efficiency of applying dE/dx separation of e/γ showers in the LAr TPC, see Sec. 5.1). Note that further rejection of this class of events is likely possible by identifying the low-energy hadronic debris near the vertex of the neutral-current interaction. The electromagnetic shower produced by the photon will be separated from, but point back to, this vertex. An observed gap between the

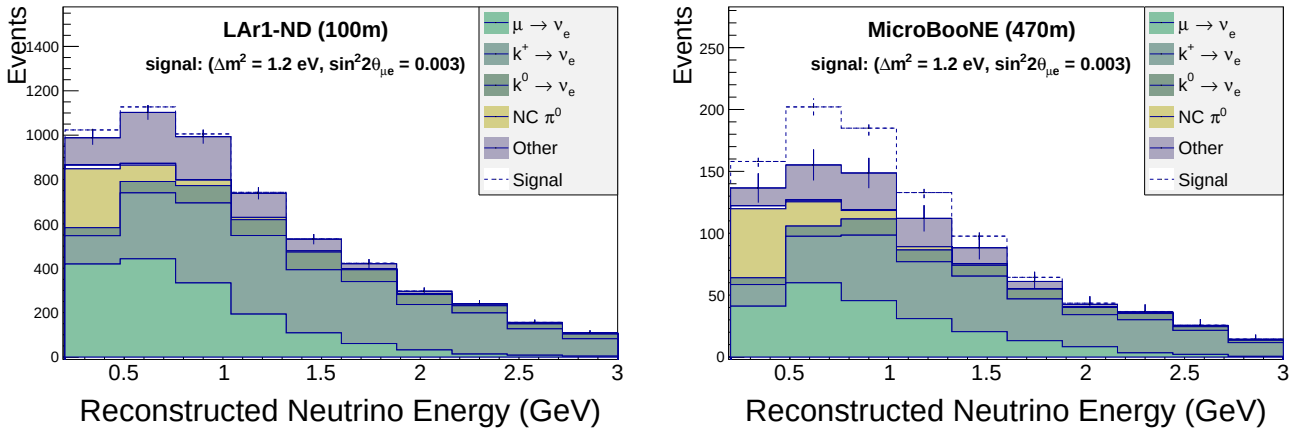

Figure 5.1: *Electron neutrino charged-current candidate distributions in LAr1-ND (left) and MicroBooNE (right) shown as a function of reconstructed neutrino energy. Oscillation signal events for parameter values near the LSND best-fit value are indicated by the dashed blue histograms.*

photon shower and the interaction vertex would allow further rejection of single photon neutral-current events.

- **NC γ production :** Neutral-current interactions resulting in photons in the final state (not from π^0 decays) are also considered as background if the photon converts within the fiducial volume and 6% of these events are accepted into the ν_e candidate sample (corresponding to the expected efficiency of applying dE/dx separation of e/γ showers in the LAr TPC). Just as in the photon production from π^0 described above, there is the additional possibility to reject these events through the identification of a separated interaction vertex which is not being utilized here.

- **ν_μ CC :** For ν_μ charged-current interactions within the fiducial volumes, we assume 0.1% are mis-identified as electron neutrino interactions based on current estimates. Such events can enter into the sample only if there is an identified electromagnetic shower and the muon is not identified. The presence of the muon, of course, tags the event as ν_μ CC.

By analyzing the conversion points of photons instead of the true neutrino interaction vertex, we accurately account for acceptance effects in the differently shaped detectors. Because the e/γ separation is performed *entirely with the first few centimeters of a shower*, differences in total shower containment do not affect the assumption that the photon identification efficiency is the same in each detector.

Figure 5.1 shows the expected ν_e candidate event distributions as a function of the

neutrino energy (reconstructed from electron and hadron kinematics, as described in Sec. 5.1) in LAr1-ND and MicroBooNE for exposures of 2.2×10^{20} and 6.6×10^{20} protons-on-target, respectively.

An example signal is included in the event distributions of Fig. 5.1. The high statistics event sample in LAr1-ND constrains the expected background event rate in MicroBooNE, reducing significantly the systematic uncertainties on the background. Figure 5.2 compares the sensitivity to a $\nu_\mu \to \nu_e$ oscillation signal under the 3+1 model of MicroBooNE alone (left) and MicroBooNE + LAr1-ND (right). The sensitivity is extracted by performing a raster scan in Δm^2 where we use the standard $\Delta\chi^2$ cuts for one (1) degree of freedom of 1.64 (one-sided), 9.00 (two-sided), and 25.0 (two-sided) to define the 90%, 3σ, and 5σ confidence level (CL) contours. The sensitivity in MicroBooNE is strengthened through the reduction of systematic errors possible with LAr1-ND. The LAr1-ND + MicroBooNE combined sensitivity covers the best-fit point to the LSND data at between 4 and 5σ.

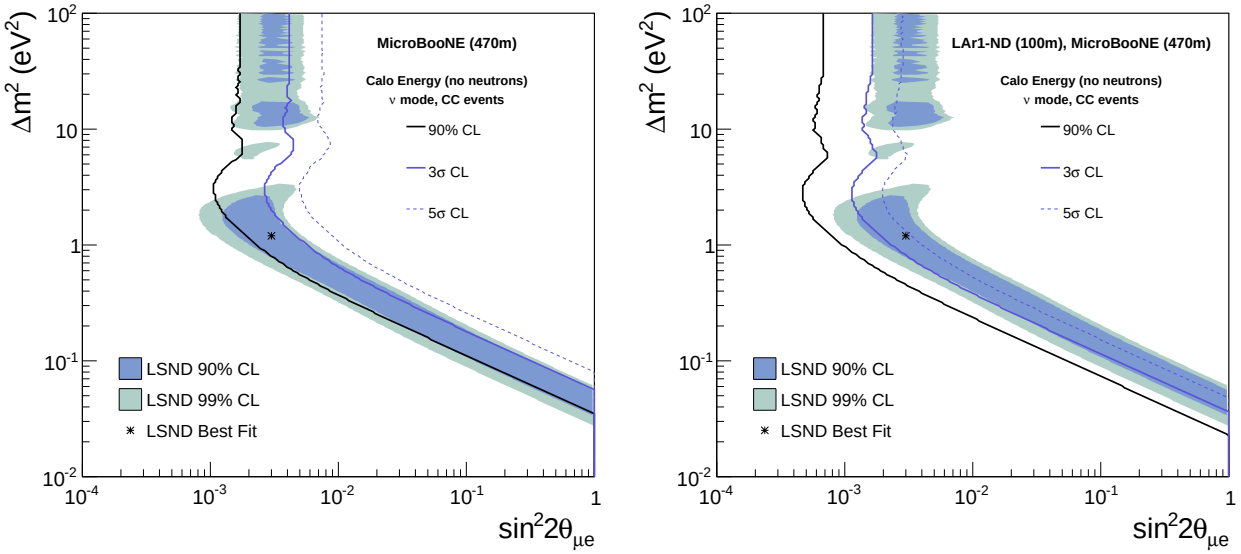

Figure 5.2: *(Left) Sensitivity to ν_e appearance in neutrino mode with 6.6×10^{20} protons on target exposure for MicroBooNE alone and assuming 20% systematic uncertainties on ν_e backgrounds. (Right) Sensitivity with the same MicroBooNE exposure and a including 2.2×10^{20} protons on target exposure for LAr1-ND. The systematics in the far detector (MicroBooNE) are taken to be the statistical uncertainties in LAr1-ND.*

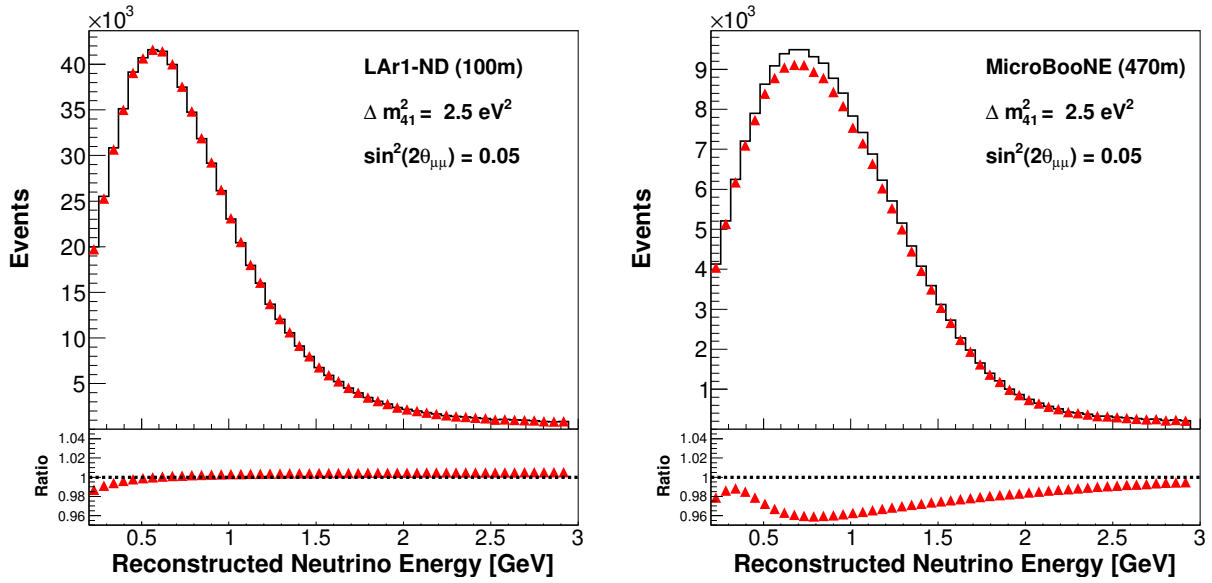

Figure 5.3: *A $\Delta m^2_{41} = 2.5\ eV^2$ ν_μ disappearance signal in LAr1-ND (left) and MicroBooNE (right). Black histograms show the predicted event distribution in the absence of oscillations. Red triangles are the observed event distributions for $\Delta m^2_{41} = 2.5\ eV^2$ and $\sin^2 2\theta_{\mu\mu} = 0.05$. The statistics shown are for 2.2×10^{20} protons on target exposure for LAr1-ND and 6.6×10^{20} protons on target for MicroBooNE. Flux and cross section errors of 15-20% would hide this signal in MicroBooNE alone, but using the observed LAr1-ND spectrum to normalize the expected rate at MicroBooNE makes it observable.*

5.2.3 ν_μ Disappearance

Any observation of ν_e appearance that is to be interpreted as a $\nu_\mu \to \nu_s \to \nu_e$ oscillation signal must be accompanied by the disappearance of ν_μ with greater or equal probability. Therefore, sensitive searches for ν_μ disappearance are an important component of the test for low-mass sterile neutrinos. In a 3+1 sterile neutrino model, that probability is given by:

$$P^{3+1}_{\nu_\mu \to \nu_x} = 1 - \sin^2 2\theta_{\mu\mu} \sin^2 \frac{\Delta m^2_{41} L}{4E} \tag{5.5}$$

where the second term is the survival probability for ν_μ as a function of L and E, the neutrino path length and energy, respectively. The search for ν_μ disappearance is a significant aspect of the physics program which is gained with this proposal because only with a near detector is there the possibility of a sensitive search for ν_μ disappearance.

Unlike the search for ν_e appearance, the search for ν_μ disappearance in MicroBooNE is not challenged by small statistics. Instead, overall normalization uncertainties on the predicted ν_μ charged-current event rate of 15-20% (from uncertainties in both the neutrino flux and interaction cross sections) obscure disappearance signals below this level. Figure 5.3 shows

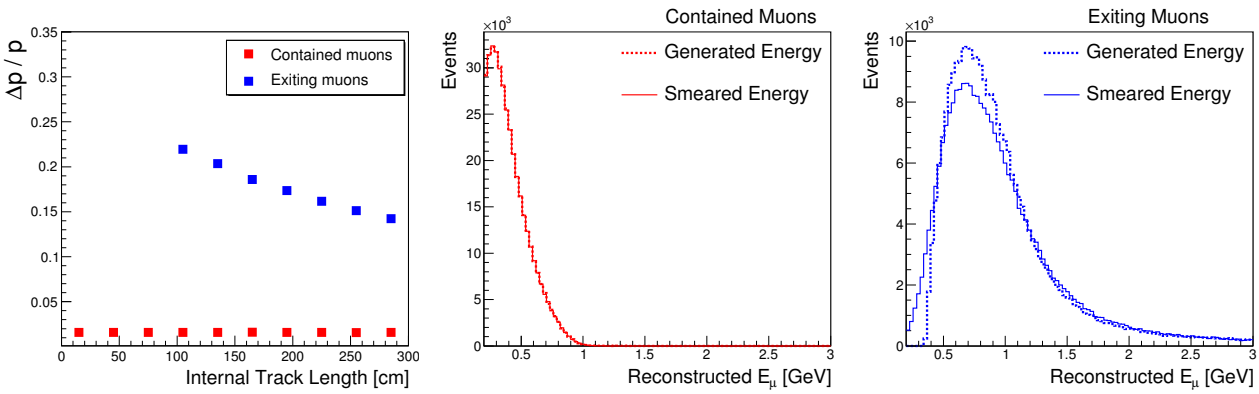

Figure 5.4: *Left: Resolutions used to smear the reconstructed muon energy for contained (red) and exiting (blue) muons [38]. These are independent of the muon energy, but the resolution for the exiting muons depends on the track length. The middle and right plots show the generated and smeared muon energy distributions for the contained and exiting sub-samples in the ν_μ CC events accepted in LAr1-ND for the disappearance analysis.*

an example oscillation signal for $\Delta m^2_{41} = 2.5$ eV^2. Due to its location close to the target, the effects of the oscillation are negligible in LAr1-ND and only at neutrino energies less than 0.5 GeV. At the MicroBooNE location, however, a significant distortion of the spectra is visible if systematics can be controlled. LAr1-ND, by providing a high statistics measurement of the ν_μ interaction rate in the beam before the on-set of an oscillation, can provide a precise prediction at MicroBooNE and enable a sensitive search for ν_μ disappearance.

An important consideration is energy smearing in the reconstructed samples since oscillation signals will appear as a modulation of the ν_μ charged-current interaction spectrum. To account for realistic smearing in LAr1-ND and MicroBooNE events, we divide the charged-current samples in each detector into a "contained" and an "exiting" sample, where the label refers to the muon track in the event and whether it leaves the TPC active volume. The energy of muons which are contained in the argon can be measured very precisely, with a resolution of ∼2%. In LAr1-ND, 45% of the muons produced in ν_μ CC events occurring in the fiducial volume are contained. For muons which exit the volume, we can use the amount of multiple scattering along the track to estimate the muon energy as demonstrated by the ICARUS collaboration [38]. They found a resolution which is independent of total energy of the muon but depends on the length of the track. In the present analysis, we require that exiting muons travel ≥1 m in the TPC active volume to ensure sufficient length over which to measure the multiple scattering of the track. Figure 5.4 shows the resolutions used to smear the muon energy as a function of track length and shows the effect for muons which stop in the argon and those which exit the volume. The 1 m track length requirement rejects

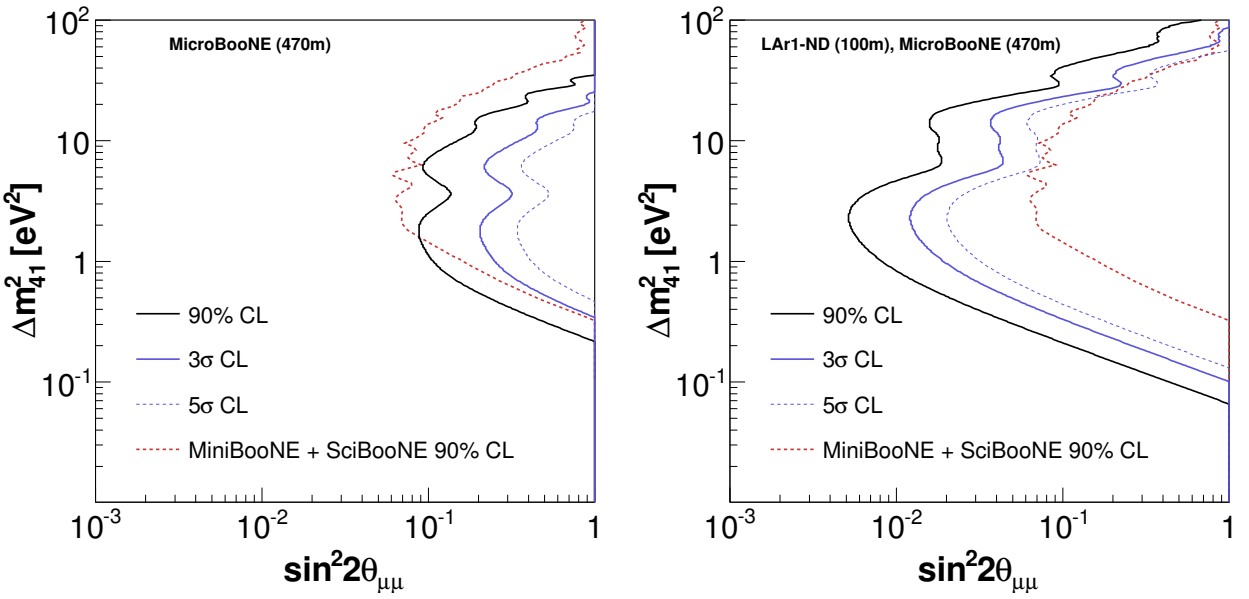

Figure 5.5: *Sensitivity to ν_μ disappearance of MicroBooNE alone (left) and including one year of neutrino running of LAr1-ND (right). In each case, the red dotted line shows the limit set by the SciBooNE + MiniBooNE combined search for ν_μ disappearance [39] for comparison. With MicroBooNE alone a 20% systematic uncertainty on the absolute ν_μ event rate is assumed.*

some exiting muon events, but in the end we are left with 373k contained muon ν_μ CC events and 265k exiting muon ν_μ CC events after LAr1-ND in 2.2×10^{20} POT of running. The true and reconstructed muon energy in these samples, which provide the un-oscillated constraint for the ν_μ disappearance analysis, are shown in Fig. 5.4. To estimate the neutrino energy, we combine the smeared muon energy and the energy of any charged final state hadrons, as described in Sec. 5.1. The hadronic energy is also smeared by 5%.

Figure 5.5 demonstrates the effectiveness of the near detector constraint on the sensitivity to ν_μ disappearance. The left panel shows the estimated sensitivity to ν_μ disappearance in the $(\Delta m^2_{41}, \sin^2 2\theta_{\mu\mu})$ plane for MicroBooNE alone assuming a 20% overall normalization uncertainty on the predicted ν_μ CC rate, and one can see that MicroBooNE alone is not competitive with existing measurements. The right panel illustrates the improvement with LAr1-ND serving as a near detector. The measurement in LAr1-ND is used to normalize the far detector spectrum in the absence of oscillations and the statistical uncertainties in the near detector determine the size of the systematics in the far detector (MicroBooNE). The sensitivity shown is for a *shape only* analysis in the far detector, where the integrated rate observed in LAr1-ND is used to normalize the predicted spectrum at MicroBooNE. In this way, any oscillation signal at the near detector is normalized out of the data. This leads to the reduced sensitivity at very high Δm^2 where rapid oscillations result in a significant, but

mostly flat reduction in the ν_μ event rate even at the near detector.

Also shown in Fig. 5.5, for comparison, is the limit set by the SciBooNE and MiniBooNE collaborations who combined data from their experiments in the same beam to search for ν_μ disappearance [39]. In addition to the larger mass (49 tons fiducial volume in LAr1-ND vs. 10.6 tons in SciBooNE) and greater exposure (2.2×10^{20} vs. 0.99×10^{20} protons on target in neutrino-mode for SciBooNE), the major advantage in the proposed combination of LAr1-ND + MicroBooNE is the use of the same detector technology when looking for a deficit or spectral distortion in the far detector relative to the near. In the combined SciBooNE + MiniBooNE analysis it is concluded that: *"The differences in the event rates in the two detectors due to flux or cross sections systematics, unlike detector systematics, tend to cancel. As a result, the largest uncertainty for the analysis is the MiniBooNE detector uncertainty"*.

By using the same technology, important detector systematics on event selection efficiencies and energy reconstruction will mostly cancel in an analysis of data from LAr1-ND and MicroBooNE and thereby increase significantly the experimental sensitivity to ν_μ disappearance signals over past experiments.

5.2.4 Probing Active to Sterile Oscillations With Neutral-Currents

A unique probe of sterile neutrino oscillations, directly sensitive to any "sterile" flavor content, is available through neutral-current (NC) neutrino interactions. In this type of search, one looks for an overall depletion of the flavor-summed event rate. As with ν_μ disappearance, this type of search is significantly less sensitive in a single-detector experiment due to large systematic uncertainties in flux and cross section. A two-detector experiment provides superior sensitivity by removing these systematic errors.

In a NC-based search, neutrino energy reconstruction is impossible because the surviving neutrino carries off an unknown amount of energy. Similarly, flavor identification is also not possible. Therefore, one relies on looking for an overall deficit of the flavor-summed event rate. We have considered here the NC π^0 channel, due to its characteristic event topology and kinematics. Unlike other NC channels, the presence of the two photons from the π^0 decay pointing back to a common vertex, with an invariant mass corresponding to $m_{\pi 0}$, provides a powerful discriminant against potential backgrounds. This yields a better understood event sample that is less susceptible to systematic errors and backgrounds.

To estimate event rates for a reconstructed NC π^0 sample at each detector location, we apply truth-based event selection cuts, including (1) a fiducial volume cut on the event vertex, (2) 100% rejection against CC events, (3) only a single π^0 present in the final state, and (4) both photons from the π^0 decay converting within the detector fiducial volume, as well as an

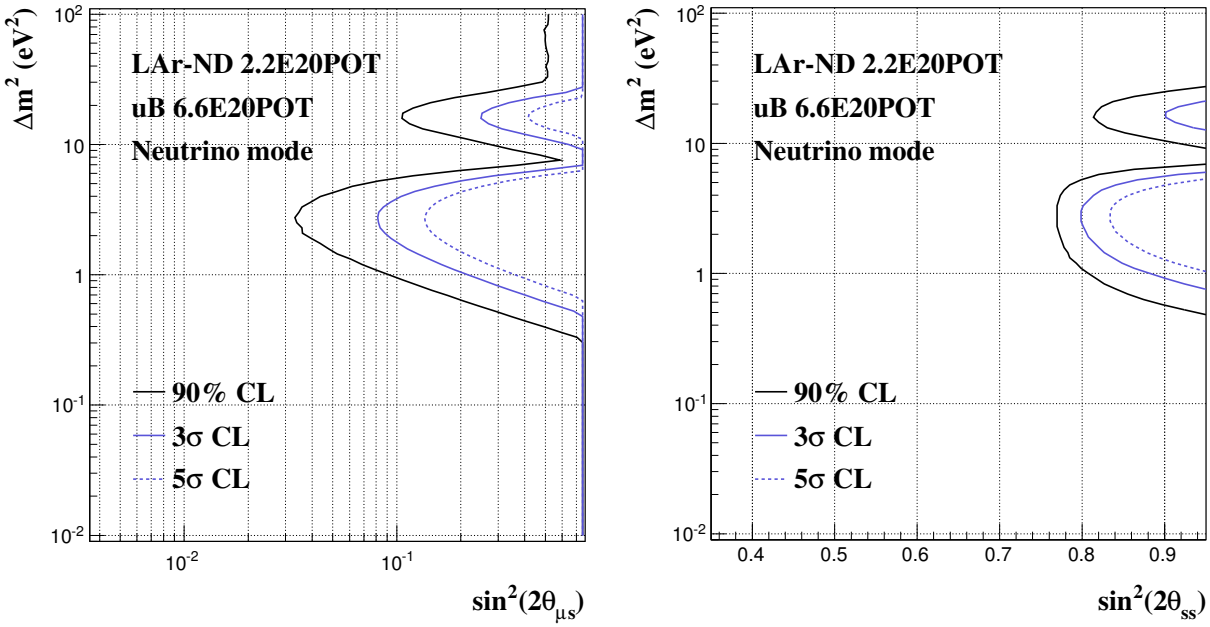

Figure 5.6: *Sensitivity to disappearance into sterile neutrinos in neutrino mode with* 6.6×10^{20} *protons on target exposure for MicroBooNE and* 2.2×10^{20} *protons on target exposure for LAr1-ND. The sensitivity assumes a fully-correlated 20% systematic uncertainty on the NC* π^0 *rate at each location. Left: The sensitivity is shown as a function of* $\sin^2(2\theta_{\mu s})$*, the* $\nu_\mu \to \nu_s$ *"appearance" probability amplitude; since the BNB is primarily a muon neutrino beam, this is the most relevant indirectly accessible amplitude from a neutral-current disappearance search. Right: The sensitivity is shown as a function of* $\sin^2(2\theta_{ss})$*, which can be thought of as the sum of* $\nu_\mu \to \nu_s$ *and* $\nu_e \to \nu_s$ *appearance amplitudes. See Sec. 5.2.4 for more details.*

additional overall reconstruction efficiency of 50%, to account for any resulting inefficiency on single-shower reconstruction and/or π^0 mass reconstruction. We expect approximately 30,000 NC π^0 interactions in LAr1-ND for 2.2×10^{20} proton on target exposure (Sec. 5.2.6). This corresponds to a <1% statistical uncertainty on a measurement of the unoscillated NC π^0 event rate. Similar LAr TPC detectors at both locations means that systematic uncertainties will largely cancel in predicting the rate at MicroBooNE, making neutral-current disappearance an excellent and complementary way to test for new physics with LAr1-ND.

Neutral-current interactions sample all active flavors and their couplings to sterile flavors are, in general, different. In a 3+1 scenario, the probability that an active neutrino $\alpha = e, \mu$ or τ survives as *any* active neutrino is approximated using the standard two-neutrino oscillation probability as

$$P_{\alpha\alpha} = 1 - 4|U_{\alpha 4}|^2|U_{s4}|^2 \sin^2 \frac{\Delta m^2_{41} L}{4E} \tag{5.6}$$

where $|U_{\alpha 4}|^2$ and $|U_{s4}|^2$ are the α and sterile (s) content of the fourth mass eigenstate. By unitarity considerations, $|U_{s4}|^2 = 1 - |U_{e4}|^2 - |U_{\mu 4}|^2 - |U_{\tau 4}|^2$. In the sensitivity estimates considered here, $|U_{\tau 4}|^2 = 0$ for simplicity.

In extracting the sensitivity contours shown in Fig. 5.6, a χ^2 surface is constructed by comparing the flavor-summed NC π^0 total predicted event rate in the absence of oscillations to that expected due to oscillations of the muon and electron neutrino flux components ($\alpha = e, \mu$) according to Eq. 5.6. The χ^2 calculation this time involves a full covariance matrix to account for an assumed fully-correlated 20% systematic uncertainty among the two detector locations, as well as statistical uncertainties. Since three different parameters are involved in the fit, $|U_{e4}|$, $|U_{\mu 4}|$, and Δm^2, a marginalization over $|U_{e4}|$ and $|U_{\mu 4}|$ is performed in terms of the parametrization $\sin^2 2\theta_{ss} = 4|U_{s4}|^2(1 - |U_{s4}|^2)$. This parameter is proportional to both the amount of sterile flavor and the amount of total active flavor in the fourth mass eigenstate, suggesting that both must be non-zero to facilitate active-sterile oscillations. This is therefore an appropriate metric for quantifying sensitivity. Following the sensitivity calculation prescription for ν_μ disappearance and ν_e appearance in the previous sections, a raster scan is then performed in the 2D plane of Δm^2 versus $\sin^2 2\theta_{ss}$.

5.2.5 Anomalous Single Photon Production

It is possible that the event excess observed by MiniBooNE at low reconstructed energies in the Booster Neutrino Beam is not due to $\nu_\mu \to \nu_e$ oscillations, but is instead comprised of an as-yet unknown source of neutral-current interactions producing single photons in the final state. Cherenkov detectors, such as MiniBooNE, are not able to distinguish electromagnetic showers initiated by photons versus by electrons. MicroBooNE, on the other hand, by applying the LAr TPC technology, will determine at ~500 m if the excess is coming from ν_e's or photons produced in (mostly ν_μ) NC interactions.

In confirming that the observed MiniBooNE excess is photons, MicroBooNE would see a few dozen events above expected backgrounds at low-energy. In this scenario, LAr1-ND at 100 m will allow to immediately confirm that the excess is intrinsic in the beam (i.e. that it is some standard, but un-modeled neutral-current interaction), and, importantly, LAr1-ND will have hundreds of events per year, as shown in Table 5.1. Such a sample will enable a measurement of this unknown reaction with much greater precision and inform the development of cross section models in this energy range to include this process with the correct rate. This will be important input for some accelerator-based neutrino experiments studying oscillations at the atmospheric Δm^2 that observe signals in the few hundred MeV energy range. In particular, a new source of single photon final states has implications for other Cherenkov detector neutrino experiments in the same energy range, such as T2K.

5.2.6 Neutrino Cross Sections

Precise cross section measurements are considered a fundamental prerequisite for every neutrino oscillation study. In the energy range of interest, as a result of competitive physical processes and complicated nuclear effects, neutrino interactions on argon include a variety of final states. These can range from the emission of multiple nucleons to even more complex topologies with multiple pions, all in addition to the leading lepton. Liquid argon TPC technology is particularly well suited to this purpose because of its excellent particle identification capability and calorimetric energy reconstruction down to very low thresholds.

LAr1-ND provides an ideal venue to conduct precision cross section measurements in the critical 1 GeV range. A novel approach based on the event categorization in terms of exclusive topologies can be used to analyze data and provide precise cross section measurements. Due to its location near the neutrino source (20-30× the flux at MicroBooNE) and relatively large mass, LAr1-ND will make measurements of neutrino interactions with high statistics, as shown in Table 5.3. In the table, we show the expected rate of events in their main experimental topologies. Included for reference, we also show the classification by physical process from Monte Carlo truth information. An exposure of one year (2.2×10^{20} POT) with LAr1-ND will provide an event sample 6-7× larger than will be available in MicroBooNE alone.

5.3 Analysis of NuMI Beam Events

A large number of neutrino events coming from the NuMI beamline will be observed by the different detectors. These events have not been included yet in the sensitivity studies presented in this proposal, but the expected event rates are presented in this section to demonstrate the great potential of analyzing the neutrino events coming from the off-axis NuMI beam.

The analysis of the NuMI events was done in the same way as the Booster beam event analysis presented previously. The fluxes presented in Section 3.2 were used to simulate the neutrino events in LAr1-ND and MicroBooNE. Figures 5.7 and 5.8 show the expected event rates for 9.0×10^{20} POT of neutrino and anti-neutrino running modes, respectively. Note that it is expected that during the NOvA era, the NuMI beam could generate up to 6×10^{20} POT/year [40]. Tables 5.4 to B.2 show the total number of NuMI events predicted for the two detectors for neutrino and anti-neutrino mode running.

A considerable number of neutrino events coming from the NuMI beam will be available for analysis. It is interesting that a large fraction of the NuMI events are at lower energies ($E < 500$ MeV). These energies are particularly important when addressing the MiniBooNE

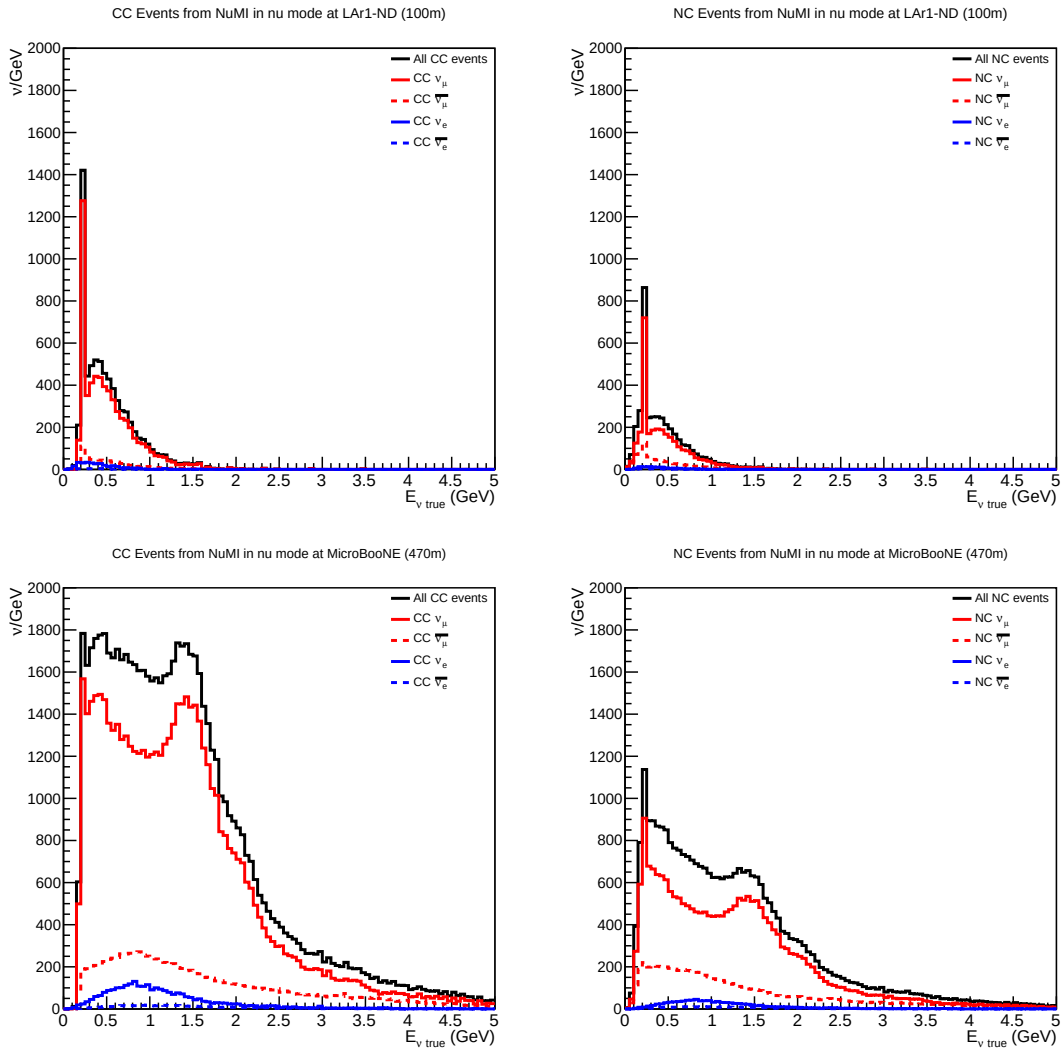

Figure 5.7: *Event rates expected from the off-axis NuMI beam in neutrino mode running at the different detector location for* 9×10^{20} *POT: Top: LAr1-ND, Middle: MicroBooNE, Bottom: LAr1-FD. The left plots show the expected CC event rates and the right plots show the expected NC event rates.*

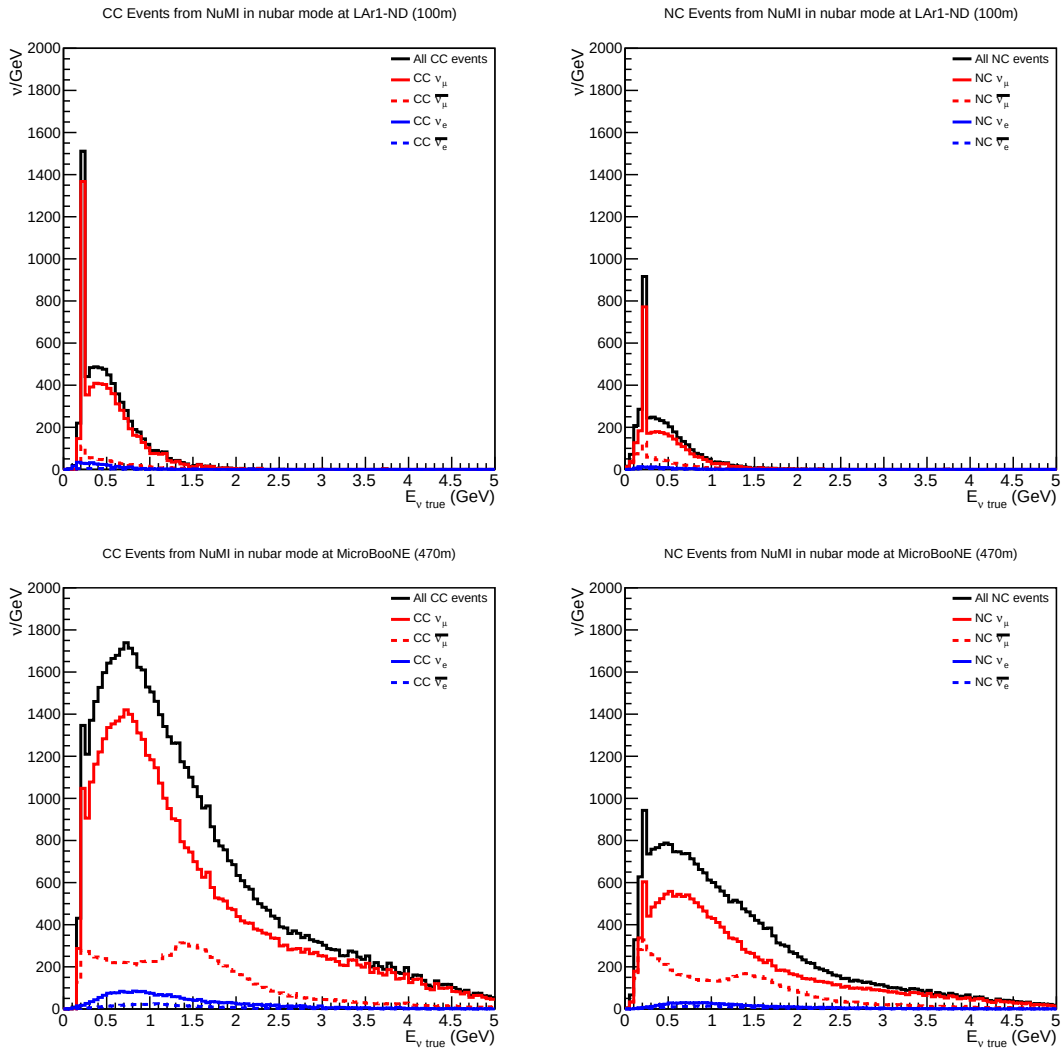

Figure 5.8: *Event rates expected from the off-axis NuMI beam in anti-neutrino mode running at the different detector location for* $9 \times 10^{20} POT$*: Top: LAr1-ND, Middle: MicroBooNE, Bottom: LAr1-FD. The left plots show the expected CC event rates and the right plots show the expected NC event rates.*

Process		**No. Events**
	ν_μ Events (By Final State Topology)	
CC Inclusive		787,847
CC 0 π	$\nu_\mu N \to \mu + Np$	535,673
	· $\nu_\mu N \to \mu + 0\text{p}$	119,290
	· $\nu_\mu N \to \mu + 1\text{p}$	305,563
	· $\nu_\mu N \to \mu + 2\text{p}$	54,287
	· $\nu_\mu N \to \mu + \geq 3\text{p}$	56,533
CC 1 $\pi^\pm$	$\nu_\mu N \to \mu + \text{nucleons} + 1\pi^\pm$	176,361
CC $\geq 2\pi^\pm$	$\nu_\mu N \to \mu + \text{nucleons} + \geq 2\pi^\pm$	14,659
CC $\geq 1\pi^0$	$\nu_\mu N \to \text{nucleons} + \geq 1\pi^0$	76,129
NC Inclusive		300,585
NC 0 π	$\nu_\mu N \to \text{nucleons}$	206,563
NC 1 $\pi^\pm$	$\nu_\mu N \to \text{nucleons} + 1\pi^\pm$	39,661
NC $\geq 2\pi^\pm$	$\nu_\mu N \to \text{nucleons} + \geq 2\pi^\pm$	5,052
NC $\geq 1\pi^0$	$\nu_\mu N \to \text{nucleons} + \geq 1\pi^0$	54,531
	ν_e Events	
CC Inclusive		5,883
NC Inclusive		2,098
Total ν_μ and ν_e Events		1,096,413
	ν_μ Events (By Physical Process)	
CC QE	$\nu_\mu n \to \mu^- \text{p}$	470,497
CC RES	$\nu_\mu N \to \mu^- N$	220,177
CC DIS	$\nu_\mu N \to \mu^- X$	82,326
CC Coherent	$\nu_\mu Ar \to \mu Ar + \pi$	3,004

Table 5.3: *Estimated event rates using GENIE (v2.8.0) in a* 2.2×10^{20} *POT exposure of LAr1-ND. In enumerating proton multiplicity, we assume an energy threshold on protons of 21 MeV. The* 0π *topologies include any number of neutrons in the event.*

low-energy excess and adding the NuMI events to the analysis could help considerably to increase the statistics.

The additional NuMI neutrino events will also significantly enlarge the statistics for cross-section measurements, especially for rarer interactions. In addition, the very low energy NuMI events (E $<$ 100 MeV) could be used to study the CC absorption reaction of ν_e on

Table 5.4: *Number of neutrino events from NuMI beam in neutrino mode in LAr1-ND (100m) for 49t for* $9 \times 10^{20} POT$.

Neutrino flavor	All events	CC events	NC events
ν_μ	9,148	6,143	3,005
$\bar{\nu_\mu}$	1,498	720	778
ν_e	430	311	119
$\bar{\nu_e}$	74	41	33
Total	11,150	7,215	3,935

Table 5.5: *Number of neutrino events from NuMI beam in anti-neutrino mode in LAr1-ND (100m) for 49t for* $9 \times 10^{20} POT$.

Neutrino flavor	All events	CC events	NC events
ν_μ	9,506	6,388	3,118
$\bar{\nu_\mu}$	1,531	735	796
ν_e	439	319	120
$\bar{\nu_e}$	84	46	38
Total	11,561	7,488	4,073

Table 5.6: *Number of neutrino events from NuMI beam in neutrino mode in MicroBooNE (470m) for 61.4t for* $9 \times 10^{20} POT$.

Neutrino flavor	All events	CC events	NC events
ν_μ	78,955	56,751	22,204
$\bar{\nu_\mu}$	17,769	10,946	6,823
ν_e	3,834	2,828	1,006
$\bar{\nu_e}$	888	569	319
Total	101,446	71,095	30,351

Table 5.7: *Number of neutrino events from NuMI beam in anti-neutrino mode in MicroBooNE (470m) for 61.4t for* $9 \times 10^{20} POT$.

Neutrino flavor	All events	CC events	NC events
ν_μ	67,861	49,060	18,801
$\bar{\nu_\mu}$	19,317	11,783	7,534
ν_e	3,320	2,452	868
$\bar{\nu_e}$	950	600	350
Total	91,449	63,895	27,554

Ar nuclei (ν_e + A(Z,N) $\rightarrow$ e^- + A(Z+1,N-1)). This interaction is crucial to understand potential supernova neutrinos and currently there is no experimental data at these energies on Ar. Based on theoretical predictions of the cross-section of this interaction [41], it was estimated that 22 and 32 events would be observed in LAr1-ND and MicroBooNE respectively for 9.0×10^{20}POT. There are many assumptions that go into the theoretical calculations of this cross-section and having data in this energy range would greatly help.

Chapter 6

Cost and Schedule

Estimates for LAr1-ND construction costs are based on recent experience at Fermilab building related LAr projects including MicroBooNE, the LBNE 35 ton membrane cryostat, and the Liquid Argon Purity Demonstrator (LAPD). Table 6.1 lists estimated costs for the major systems of the detector. The total project cost for the detector, modifications to the conventional facilities, and project management is estimated at $13M.

Item	**Estimated Cost**
1. Enclosure	$0.3M
2. Cryostat	$2.5M
3. Cryogenic System	$3.0M
4. Time Projection Chamber (TPC)	$2.0M
5. Front-end TPC Electronics	$1.5M
6. Light Detection System	$0.5M
7. Readout, Trigger and DAQ	$0.5M
8. Integration and Installation	$1.0M
Total Construction Costs	$11.3M
Project Management at 15%	$1.7M
Project Total	$13M

Table 6.1: *Estimated costs for the construction of LAr1-ND are based on experience with the MicroBooNE and LBNE 35 ton prototype construction costs.*

1. **Enclosure:** This detector will use the existing SciBooNE enclosure. Tasks and costs include what is needed to prepare the enclosure to accommodate a cryogenic detector. This includes some structural work for an interior wall, mechanical support structures

above the detector and an upgrade to the electrical service to the building to support operation of the cryogencis.

2. **Cryostat:** The cryostat will use the membrane technology. Costs are based on scaling from the LBNE 35 ton prototype recently built at Fermilab.

3. **Cryogenic System:** The cryogenic system design is based on experience with the designs and operation of the systems for LAPD, MicroBooNE and 35 ton. Lessons learned and improvements for cost and performance have been incorporated into the estimate.

4. **TPC:** The design and fabrication of the parts of the TPC, including installation fixtures and all hardware are based on the experience from construction of the MicroBooNE TPC; this estimate includes on-site assembly and installation labor costs.

5. **TPC Front-end Electronics:** The front-end electronics includes charge collection, amplification and digitization of signals from the TPC. The M&S and design costs are based on experience from the MicroBooNE system.

6. **Light Detection System:** LAr1-ND will develop an innovative approach to light detection using new ideas that have been initiated in the context of R&D for the LBNE far detector.

7. **Readout, Trigger and DAQ:** The Readout and Trigger requirements for LAr1-ND are under development. The DAQ system will be based on the system that has been developed for MicroBooNE. Costs are estimated from the M&S and labor costs for the development of the similar systems in MicroBooNE.

8. **Integration and Installation:** Cost and schedule for assembly and installation are estimated based on experience to date in MicroBooNE.

We are actively exploring opportunities and following up on interests for collaboration with non-US groups both through participation in the experiment and through significant in-kind hardware contributions. Many in the international community are interested in the LAr neutrino program being planned in the U.S. and LAr1-ND offers a near-term, modest-scale opportunity to enter that larger program. The building of the LAr1-ND collaboration is a very active and important aspect of the on-going work to develop the project. We will be happy to provide an up-to-date picture at the time of the PAC meeting in January.

Based on experience from MicroBooNE, the detector construction could be completed in two years. A construction start on the 2015 time scale maximizes the physics potential in Phase-I within the existing Fermilab program by making it possible to run the LAr1-ND

detector concurrently with MicroBooNE toward the end of the already planned neutrino-mode running.

Chapter 7

Conclusions

The hints for new physics at short-baselines are being explored by new experiments in the planning stages and near running worldwide. Whether or not we find new physics, the anomalies must be resolved definitively. Fermilab will have the first opportunity to address these with MicroBooNE. LAr1-ND enables the full interpretation of a MicroBooNE signal, be it electrons or photons, by providing a high statistics measurement at nearer baseline on a rapid time scale. LAr1-ND would also be an important element for measurements in antineutrino mode by serving as a near detector for the LAr1 far detector in a possible future phase of the Fermilab short-baseline neutrino program.

This proposal describes LAr1-ND and the compelling physics it brings first in Phase-I and next towards the full LAr1 program. In addition, LAr1-ND serves as a next step in the development toward large-scale LAr TPC detectors. Its development goals will encompass testing existing and possibly innovative designs for LBNE while at the same time providing a training ground for teams working towards LBNE combining timely neutrino physics with experience in detector development.

The Collaboration hopes to be considered for Stage 1 approval and to receive encouragement from the Fermilab Director to develop this Proposal into a technical design.

Appendix A

Dark Matter Searches with Booster Beam Off-Target Running

There is an abundance of evidence in support of dark matter from astrophysical and cosmological observations. The baryonic matter comprises only about 20% of matter in the Universe, and the rest is in a form of dark matter which does not interact via usual Standard Model interactions. The experimental hunt for dark matter candidates is on and a number of experiments are trying to directly observe dark matter particles.

Direct dark matter searches typically look for nuclear recoil with dark matter in the halo. These experiments have been focused on dark matter particles with mass of few GeV or above and rapidly lose sensitivity at lower mass. However, recent theoretical work has revealed that sub-GeV dark matter particles are highly viable candidates [42, 43, 44, 45]. The present limits, and the lack of evidence for new particles at weak scale found at the LHC further motivate the exploration of the low mass region.

The simplest, most generic extension of the Standard model that includes sub-GeV dark matter and satisfies constraints coming from cosmology, astrophysics and particle physics includes a massive U(1) vector mediator (V^μ). The mediator couples via kinetic mixing with hypercharge, which leads to kinetic mixing with the photon below the weak scale. A complex scalar particle χ charged under the new U(1) vector is a dark matter candidate. Incidentally, the vector particle would give contribution to the anomalous magnetic moments of Standard Model fermions and potentially explains the anomalous muon g-2 result [46, 47].

At present, several experiments are starting to probe the sub-GeV region [48, 49, 50]. Their focus is on the visible decays of the vector particle into Standard Model particles. This limits these searches to models with $m_V < 2m_\chi$. The other side with $m_V > 2m_\chi$ is equally interesting, but even less explored experimentally. The invisible decay mode $m_V \rightarrow 2m_\chi$

escapes many of the existing limits and active searches.

We discuss here the sensitivity of LAr1-ND to sub-GeV dark matter particles. An intense proton beam, like BNB, coupled with a sensitive neutrino detector is an excellent setup to search for a low mass dark matter [51]. The dark matter particles are produced through decays of mesons with large radiative branching such as π^0 and η, and can subsequently be detected via elastic scattering on nucleons and electrons in the detector. This makes the experiment a sensitive probe in the $m_V < 2m_\chi$ regime.

The major background to a dark matter search in LAr1-ND comes from neutrino neutral-current elastic (NCE) events. The dark matter events will have a similar signature in the detector as NCE neutrino scattering events. Reducing this neutrino background is crucial to boost the sensitivity. This can be achieved in a beam off-target configuration where reduction of neutrino flux by a factor of 70 is expected. In this configuration, the beam is steered directly on to the absorber. Secondary charged pions are stopped in the absorber causing reduction of the neutrino flux, while short lived π^0s and ηs still give rise to dark matter particles. A similar run is being proposed with the MiniBooNE detector [52].

Due to its proximity to the beam absorber, the number of signal events in LAr1-ND will be much higher compared to MiniBooNE or MicroBooNE, the two experiments that could also utilize BNB beam off-target running. The LAr1-ND will therefore have better sensitivity than either of those two experiments. Additionally, it will provide important information on how the potential signal scales with distance from the source.

Two channels can be used to search for dark matter particles, scattering on nucleons and scattering on electrons. While the electron channel will have worse statistics, the background in that sample will be much smaller.

Figure A.1 shows the expected number of signal events in the nucleon channel. The light blue band indicates a region where the g-2 anomaly is alleviated with these light dark matter particles. Scaling from the numbers in Table 5.3, the total expected number of NC events in beam off-target mode is ∼1600. This assumes exposure corresponding to 2×10^{20} POT, 60% efficiency for NC event selection, and reduction of neutrino flux by 70. Assuming a 10% systematic error this means that the 90% CL will lay where we expect ∼270 event excess, well below the g-2 band. For illustration, at a point in the middle of the g-2 band that intersects with the thermal abundance curve ($M_\chi \sim 10 - 20$ MeV) one expects over 5000 signal events.

In the electron channel, it is expected that the signal will be significantly reduced. However, the scattered electron will be in a very forward direction. Requiring $\cos\theta_{beam} > 0.99$ reduces background by two orders of magnitude, while keeping the signal. The search in this channel is complementary to the nucleon channel.

We discussed here the sensitivity within a simple generic model, however the experimental search with LAr1-ND is more general. The experiment will be sensitive to any anomalous signal in the neutral-current channel. With many advantages of the liquid argon technology, such as excellent event reconstruction, background rejection, lower systematic errors, and close proximity to the beam absorber, the experiment will be the most sensitive probe to sub-GeV dark matter in the BNB.

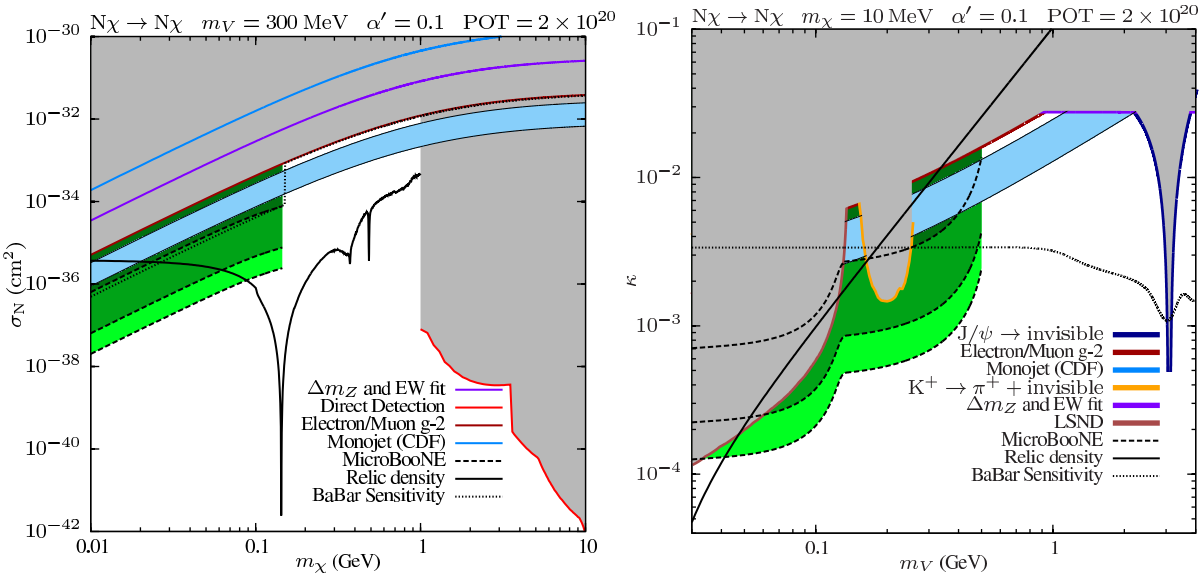

Figure A.1: *Expected sensitivities to sub-GeV dark matter for LAr1-ND. Shown is the nucleon-dark matter scattering cross section vs dark matter mass M_χ (left) and mixing angle vs vector mass M_V. The plots assume $\alpha' = 0.1$ and 2×10^{20} protons on target. The light blue region indicates where the current $\sim 3\sigma$ discrepancy in $(g\text{-}2)_\mu$ is alleviated by 1-loop corrections from the vector mediator [46, 47]. The solid black line shows points where the present dark matter relic density matches observation. The green colors indicate expected number of events 1-10 (light green), 10-1000 (green), and more than 1000 (dark green). Also shown are the present constraints [53, 54, 55, 56, 57, 58]. Figures courtesy P. deNiverville.*

Appendix B

Phase II: Three LAr TPC Detector Configuration

LAr1-ND presents a compelling physics program and an excellent opportunity to continue the development of LAr TPC technology in a running neutrino experiment. The near detector can be constructed quickly and at modest cost, and, in combination with MicroBooNE, will be able to make important statements regarding existing anomalies seen in neutrinos and record more than 1M neutrino interactions per year for studying neutrino-argon interactions.

LAr1-ND can also be thought of as the next phase in the development of a world-class program of short-baseline accelerator-based neutrino physics at Fermilab. The addition of a large (kton-scale) detector, LAr1-FD, at a longer baseline (∼700 m) would address oscillations in anti-neutrinos and make precision measurements of sterile neutrino oscillations if they are discovered. This three detector configuration, depicted in Fig. 1.2, is extremely powerful for addressing this physics, with LAr1-ND measuring the unoscillated neutrino fluxes to constrain systematic errors, a large-scale far detector measuring an oscillation signal with excellent significance and high statistics, and a signal in MicroBooNE in the middle to confirm the interpretation as new physics.

The LAr1 program will definitively address the short baseline anomalies observed by MiniBooNE in both neutrino and anti-neutrino mode.

Figure B.1 depicts the evolution of the oscillation probability with distance for oscillations in a 3+1 model occurring at $\Delta m^2_{41} = 1$ eV^2. The probability is shown for the Booster Neutrino Beam peak neutrino energy, 700 MeV. The vertical lines indicate the locations of the detectors and illustrate the ability to measure the changing oscillation with three detectors. This will provide a powerful method for the interpretation of any observed signals within an oscillation model. Two additional things to note. First, for Δm^2 less than a

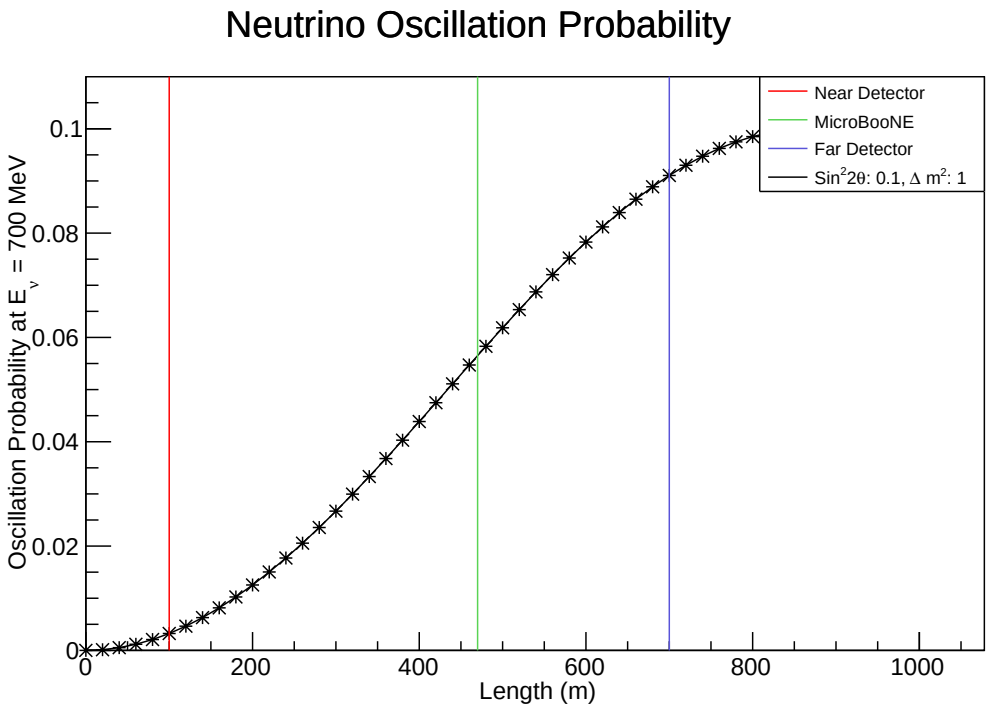

Figure B.1: *ν_μ disappearance probability at $E_\nu = 700$ MeV as a function of distance in a sterile neutrino model with $\Delta m^2 = 1$ eV^2 and $\sin^2 2\theta_{\mu\mu} = 0.1$. The vertical colored lines indicate the proposed locations of LAr1-ND, MicroBooNE and LAr1-FD.*

few eV^2, the location of LAr1-ND at 100 m is ideal for sampling the neutrino flux before the onset of any significant oscillation. This, and the factor 15 higher event rate compared to MicroBooNE, makes LAr1-ND a critical aspect of the strength of the overall program. Second, significant sensitivity is regained for large values of Δm^2 (≥ 10 eV^2) when performing a shape-only analysis relative to the 2-detector configuration.

B.1 ν_e and $\bar{\nu}_e$ Appearance

Figure B.2 shows how the higher sterile oscillation probability at 700 m and the large mass of the far detector allows for high event rates with large signal to background ratios in both neutrino and anti-neutrino mode. The addition of the far detector greatly increases the reach in sensitivity of the short baseline ν_e appearance search, as seen in figure B.3. The full LAr1 program has the ability to rule out the full LSND allowed parameter space with 5σ significance in neutrinos and anti-neutrinos or to make a discovery and measure oscillations

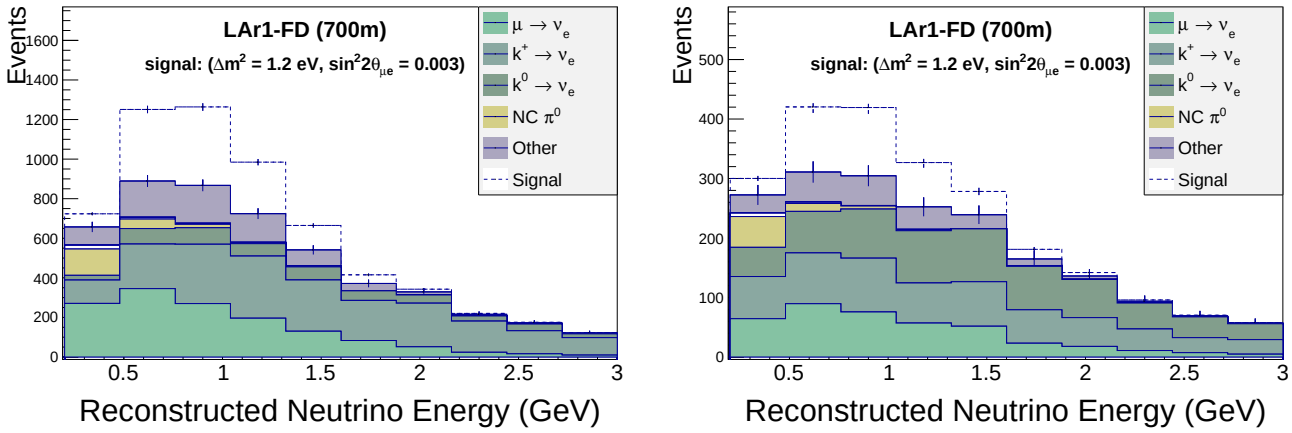

Figure B.2: *Expected event rates at a 1 kiloton liquid argon TPC located at 700m from the Booster Beam Target. On the left is neutrino mode, assuming* 6.6×10^{20} *POT, and on the right is anti-neutrino mode for* 10×10^{20} *POT.*

with good precision.

B.2 ν_μ and $\bar{\nu}_\mu$ Disappearance

Figure B.4 shows the sensitivity to ν_μ disappearance through charged-current interactions using LAr1-ND, MicroBooNE and LAr1-FD (1kton far detector at 700 m). This is the shape-only sensitivity to be compared to the plot in Fig. 5.5. This configuration enables 5σ sensitivity down to a few percent ν_μ disappearance in the $\Delta m^2 = 1$ eV^2 region.

B.3 NuMI Beam Events in LAr1-FD

The LAr1-FD detector would be only 6° off-axis on the NuMI beam and the large volume of this detector would observe a very large amount of NuMI neutrino events. The flux at the LAr1-FD is shown in Section 3.2. The expected rates simulated from these fluxes are shown in Tables B.1 and B.2 as well as in Figures B.5 and B.6.

The NuMI statistics in the LAr1-FD are extremely large (similar rates of NuMI events than from the Booster beam) and once again, a large fraction of these events are at lower energies (E $<$ 500 MeV). This detector would be even more useful for the very low energy cross-section for CC absorption mentioned in Section 5.3. For this particular cross-section, it is predicted that LAr1-FD would observe 194 events for 9.0×10^{20} POT. Considering that the

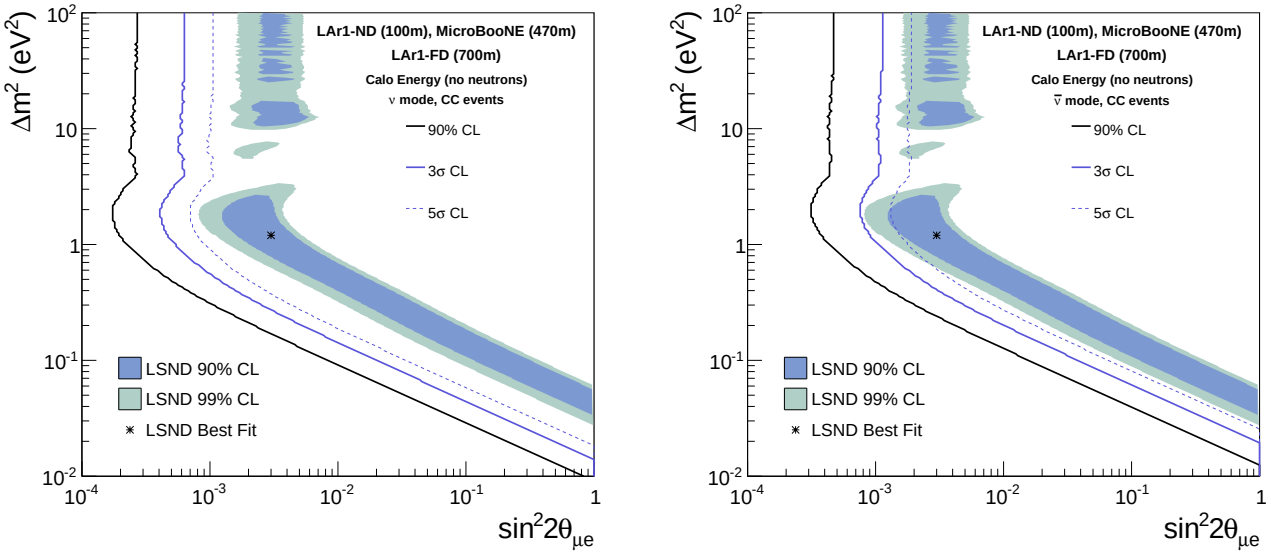

Figure B.3: *Sensitivity to ν_e appearance with the full LAr1 experiment, a program of three LAr TPC detectors on the Booster Neutrino Beamline at Fermilab, including LAr1-ND, MicroBooNE and LAr1-FD (1kton far detector). This calculation assumes 6.6e20 POT for neutrino mode, and 10e20 POT for anti-neutrino mode.*

NuMI beam is expected to produce up to 6.0×10^{20} POT/year, running LAr1-FD for three years would give a significant sample of events for this interaction crucial for supernova neutrino studies.

The higher energy NuMI neutrino events in LAr1-FD will be extremely relevant for future long baseline experiments such as LBNE. The number of NuMI events in this detector coming from NuMI will be as large as the number of events coming from the Booster beam in neutrino running mode, assuming that the NuMI beam runs at 6×10^{20} POT/year. In the case of anti-neutrino running, NuMI events will be double the statistics coming from the Booster beam.

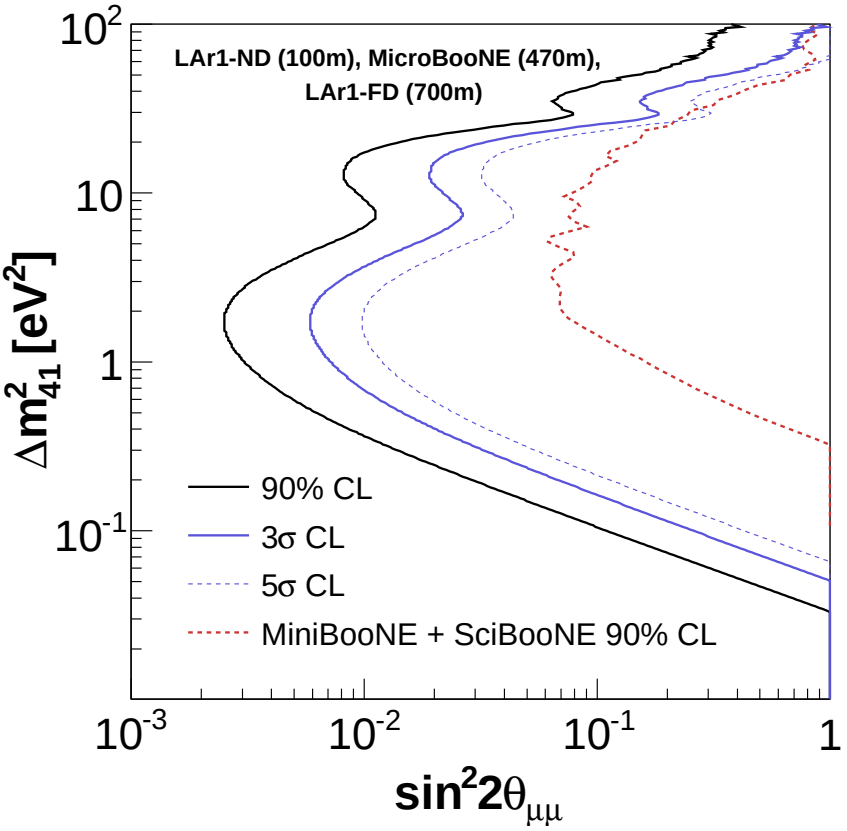

Figure B.4: *Sensitivity to ν_μ disappearance with the full LAr1 experiment, a program of three LAr TPC detectors on the Booster Neutrino Beamline at Fermilab including LAr1-ND, MicroBooNE and LAr1-FD (1kton far detector at 700 m)*

Table B.1: *Number of neutrino events from NuMI beam in neutrino mode in LAr1-FD (700m) for 1 kt for $9 \times 10^{20} POT$.*

Neutrino flavor	All events	CC events	NC events
ν_μ	1,206,770	872,937	333,833
$\bar{\nu_\mu}$	261,104	164,183	96,921
ν_e	58,692	43,405	15,287
$\bar{\nu_e}$	13,325	8,690	4,635
Total	1,539,891	1,089,215	450,677

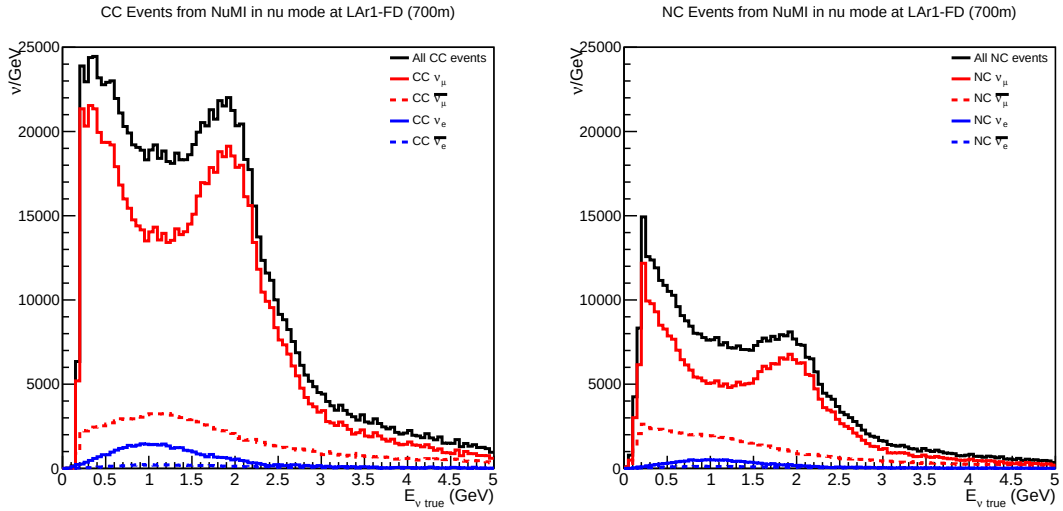

Figure B.5: *Event rates expected from the off-axis NuMI beam in neutrino mode running for* 9×10^{20} *POT for the LAR1-FD. The left plot shows the expected CC event rates and the right plot shows the expected NC event rates.*

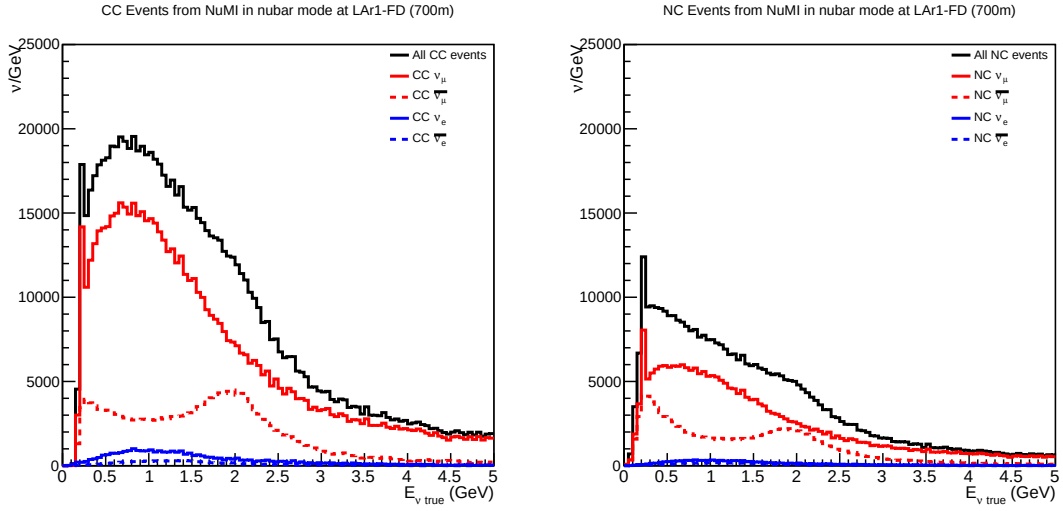

Figure B.6: *Event rates expected from the off-axis NuMI beam in anti-neutrino mode running for* 9×10^{20} *POT for the LAR1-FD. The left plot shows the expected CC event rates and the right plot shows the expected NC event rates.*

Table B.2: *Number of neutrino events from NuMI beam in anti-neutrino mode in LAr1-FD (700m) for 1 kt for* $9 \times 10^{20} POT$.

Neutrino flavor	All events	CC events	NC events
ν_μ	941,910	684,049	257,861
$\bar{\nu_\mu}$	303,661	189,003	114,659
ν_e	44,662	32,994	11,668
$\bar{\nu_e}$	15,114	9,749	5,364
Total	1,305,347	915,794	389,552

Bibliography

[1] Super-Kamiokande Collaboration, Phys. Rev. Lett. **81** (1998) 1562-1567; SNO Collaboration, Phys. Rev. Lett. **89** (2002) 011301; KamLAND Collaboration, Phys. Rev. Lett. **94** (2005) 081801; MINOS Collaboration, Phys. Rev. Lett. **101** (2008) 131802.

[2] Double Chooz Collaboration, Phys. Rev. **D86** (2012) 052008; RENO Collaboration, Phys. Rev. Lett. **108** (2012) 191802; Daya Bay Collaboration, Phys. Rev. Lett. **108** (2012) 171803; T2K Collaboration, Phys. Rev. Lett. **107** (2011) 041801; MINOS Collaboration, Phys. Rev. **D82** (2011) 051102.

[3] LBNE Collaboration, "Scientific Opportunities with the Long-Baseline Neutrino Experiment", hep-ex/1307.7335, (2013).

[4] S. Davidson, E. Nardi, Y. Nir, "Leptogenesis", Physics Reports, Volume 466, Issues 4-5, 105-177 (2008).

[5] K. N. Abazajian et al., "Light Sterile Neutrinos: A White Paper", hep-ph/1204.5379 (2012).

[6] MicroBooNE Experiment, http://www-microboone.fnal.gov/.

[7] LAr1 Letter of Intent. http://www.fnal.gov/directorate/program_planning/June2012Public/P-1030_LAR1_LoI_wAuthors.pdf

[8] R. Guenette for the LAr1 Collaboration, "LAr1: Addressing the Short-Baseline Anomalies". http://if-neutrino.fnal.gov/whitepapers/lar1.pdf.

[9] C. Rubbia, "The Liquid Argon Time Projection Chamber: A New Concept for Neutrino Detectors", CERN-EP/77-08 (1977).

[10] MiniBooNE Collaboration, A. A. Aguilar-Arevalo et al., "A Search for Electron Neutrino Appearance at the $\Delta m^2 \sim 1$ eV^2 Scale," Phys. Rev. Lett. **98** (2007) 231801.

[11] MiniBooNE Collaboration, A. A. Aguilar-Arevalo et al., "Unexplained Excess of Electron-Like Events From a 1 GeV Neutrino Beam." Phys. Rev. Lett. **102** (2009) 101802.

[12] J. Kopp et al., "Sterile Neutrino Oscillations: The Global Picture". hep-ph/1303.3011 (2013).

[13] A. Aguilar-Arevalo *et al.* [LSND Collaboration], "Evidence for neutrino oscillations from the observation of anti-neutrino(electron) appearance in a anti-neutrino(muon) beam," Phys. Rev. D **64**, 112007 (2001) [hep-ex/0104049].

[14] MiniBooNE Collaboration, A. A. Aguilar-Arevalo et al., "Improved Search for $\bar{\nu}_\mu \to \bar{\nu}_e$ Oscillations in the MiniBooNE Experiment", Phys. Rev. Lett. 110 (2013) 161801.

[15] MiniBooNE Collaboration, A. A. Aguilar-Arevalo et al., "A Search for Electron Anti-Neutrino Appearance at the $\Delta m^2 \sim 1eV^2$ Scale", Phys. Rev. Lett. 103 (2009) 111801.

[16] T. A. Mueller et al., "Improved Predictions of Reactor Antineutrino Spectra", Phys. Rev. **C83** (2011) 054615.

[17] P. Huber, "On the Determination of Antineutrino Spectra From Nuclear Reactors", Phys. Rev. **C84** (2011) 024617.

[18] G. Mention et al., "The Reactor Antineutrino Anomaly", Phys. Rev. **D83** (2011) 073006.

[19] W. Hampel *et al.* [GALLEX Collaboration], "Final results of the Cr-51 neutrino source experiments in GALLEX," Phys. Lett. B **420**, 114 (1998). , J. N. Abdurashitov *et al.* [SAGE Collaboration], "Measurement of the response of the Russian-American gallium experiment to neutrinos from a Cr-51 source," Phys. Rev. C **59**, 2246 (1999) [hep-ph/9803418].

[20] MiniBooNE Collaboration, "The Neutrino Flux prediction at MiniBooNE", arXiv:0806.1449 [hep-ex], Phys. Rev. D79 (2009) 072002

[21] HARP Collaboration, M.G. Catanesi et al., "Measurement of the Production Cross Section of Positive Pions in the Collision of 8.9 GeV/c Protons on Beryllium", Eur. Phys. J. **C52** 29-53 (2007).

[22] F. Arneodo [ICARUS Collaboration], "The ICARUS T600 liquid Argon time projection chamber," Nucl. Instrum. Meth. A **525**, 118 (2004).

[23] C. Anderson et al. [ArgoNeuT Collaboration], "The ArgoNeuT detector in the NuMI low-energy beam line at Fermilab", JINST **7**, P10019 (2012) [arXiv: 1205.6747 [physics.ins-det]].

[24] Fermilab Long Baseline Neutrino Experiment, http://lbne.fnal.gov/.

[25] B. Rebel, M. Adamowski, W. Jaskierny, H. Jostlein, C. Kendziora, R. Plunkett, S. Pordes and R. Schmitt *et al.*, "Results from the Fermilab materials test stand and status of the liquid argon purity demonstrator," J. Phys. Conf. Ser. **308**, 012023 (2011).

[26] T. Briese, L. Bugel, J. M. Conrad, M. Fournier, C. Ignarra, B. J. P. Jones, T. Katori and R. Navarrete-Perez *et al.*, "Testing of Cryogenic Photomultiplier Tubes for the MicroBooNE Experiment," JINST **8**, T07005 (2013) [arXiv:1304.0821 [physics.ins-det]].

[27] "Demonstration of a Lightguide Detector for Liquid Argon TPCs," L. Bugel, J.M. Conrad, C. Ignarra, B.J.P. Jones, T. Katori, T. Smidt, H.-K. Tanaka, arXiv:1101.3013 [physics.ins-det] , Nucl. Inst. Meth., 640:1, 69, 2011.

[28] C. S. Chiu, C. Ignarra, L. Bugel, H. Chen, J. M. Conrad, B. J. P. Jones, T. Katori and I. Moult, "Environmental Effects on TPB Wavelength-Shifting Coatings," JINST **7**, P07007 (2012) [arXiv:1204.5762 [physics.ins-det]].

[29] B. J. P. Jones, J. K. VanGemert, J. M. Conrad and A. Pla-Dalmau, "Photodegradation Mechanisms of Tetraphenyl Butadiene Coatings for Liquid Argon Detectors," JINST **8**, P01013 (2013) [arXiv:1211.7150 [physics.ins-det]].

[30] B. Baptista, L. Bugel, C. Chiu, J. M. Conrad, C. M. Ignarra, B. J. P. Jones, T. Katori and S. Mufson, "Benchmarking TPB-coated Light Guides for Liquid Argon TPC Light Detection Systems," arXiv:1210.3793 [physics.ins-det].

[31] S. Mufson and B. Baptista, "Light guide production for LBNE and the effects of UV exposure on VUV waveshifter efficiency," JINST **8**, C09012 (2013).

[32] Preliminary analysis shown here is by D. Whittington, IU.

[33] Preliminary analysis shown here is by Z. Moss, MIT.

[34] B. J. P. Jones, C. S. Chiu, J. M. Conrad, C. M. Ignarra, T. Katori and M. Toups, "A Measurement of the Absorption of Liquid Argon Scintillation Light by Dissolved Nitrogen at the Part-Per-Million Level," JINST **8**, P07011 (2013) [Erratum-ibid. **8**, E09001 (2013)] [arXiv:1306.4605 [physics.ins-det]].

[35] C.Andreopoulos et al., "The GENIE Neutrino Monte Carlo Generator", Nucl. Instrum. Meth. **A614** (2010) 87-104.

[36] LArSoft Wiki : https://cdcvs.fnal.gov/redmine/projects/larsoftsvn/wiki E. D. Church, "LArSoft: A Software Package for Liquid Argon Time Proportional Drift Chambers", arXiv:1311.6774 [physics.ins-det]

[37] S. Agostinelli et al., "Geant4 - A Simulation Toolkit", Nucl. Instrum. Meth. **A506** (2003) 250-303.

[38] A. Ankowski et al, "Measurement of Through-Going Particle Momentum By Means Of Multiple Scattering With The ICARUS T600 TPC ICARUS Collaboration", Eur. Phys. J., **C48** 667-676 (2006).

[39] K. B. M. Mahn et al. (MiniBooNE and SciBooNE Collaborations), "Dual Baseline Search for muon neutrino disappearance at 0.5 eV^2 $< \Delta m^2 <$ 40 eV^2 ", Phys. Rev. D 85, 032007 (2012).

[40] NOvA Collaboration, Proposal, http://nova-docdb.fnal.gov/cgi-bin/ShowDocument?docid=593

[41] E. Kolbe, K Langanke, G. Martinez-Pinedo, P. Vogel "Neutrino-nucleus reactions and nuclear structure" J. Phys. G: Nucl. Part. Phys. **29** (2003) 2569-2596

[42] N. Arkani-Hamed *et al.*, Phys. Rev. D 79, 015014 (2009) arXiv:0810.0713

[43] B. Batell, M. Pospelov and A. Ritz, Phys. Rev. D 80, 095024 (2009) arXiv:0906.5614;

[44] P. deNiverville, M. Pospelov and A. Ritz, Phys. Rev. D 84, 075020 (2011) arXiv:1107.4580;

[45] P. deNiverville, D. McKeen and A. Ritz, Phys. Rev. D 86, 035022 (2012) arXiv:1205.3499;

[46] P. Fayet, Phys. Rev. D 75, 115017 (2007) arxiv:hep-ph/0702176;

[47] M. Pospelov, Phys. Rev. D 80, 095002 (2009) arXiv:0811.1030;

[48] APEX http://hallaweb.jlab.org/experiment/APEX/index.html

[49] DarkLight experiment arxiv:1307.4432

[50] Heavy Photon Search http://www.jlab.org/exp_prog/proposals/11/PR12-11-006.pdf

[51] A. A. Aguilar-Arevalo *et al.*, arxiv:1211.2258 (2012).

[52] A. A. Aguilar-Arevalo *et al.*, Proposal presented at this PAC meeting.

[53] J. L. Hewett, H. Weerts, R. Brock, J. N. Butler, B. C. K. Casey, J. Collar, A. de Govea and R. Essig et al., arXiv:1205.2671 [hep-ex].

[54] G. Angloher, S. Cooper, R. Keeling, H. Kraus, J. Marchese, Y. A. Ramachers, M. Bruckmayer and C. Cozzini et al., Astropart. Phys. 18, 43 (2002).

[55] J. Angle et al. [XENON10 Collaboration], Phys. Rev. Lett. 107, 051301 (2011) [arXiv:1104.3088 [astroph.CO]].

[56] I. M. Shoemaker and L. Vecchi, Phys. Rev. D 86, 015023 (2012) [arXiv:1112.5457 [hep-ph]].

[57] M. Ablikim et al. [BES Collaboration], Phys. Rev. Lett. 100, 192001 (2008) [arXiv:0710.0039 [hep-ex]].

[58] J. Barreto et al. [DAMIC Collaboration], Phys. Lett. B 711, 264 (2012) [arXiv:1105.5191 [astro-ph.IM]].